



Available online at www.sciencedirect.com

ScienceDirect

Geochimica et Cosmochimica Acta 235 (2018) 189–207

**Geochimica et
Cosmochimica
Acta**

www.elsevier.com/locate/gca

Mg isotope response to dolomitization in hinterland-attached carbonate platforms: Outlook of $\delta^{26}\text{Mg}$ as a tracer of basin restriction and seawater Mg/Ca ratio

Or M. Bialik^{a,*}, Xiaomin Wang^b, Shugao Zhao^b, Nicolas D. Waldmann^a, Ran Frank^c, Weiqiang Li^{b,*}

^a The Dr. Moses Strauss Department of Marine Geosciences, Charney School of Marine Sciences, University of Haifa, Mount Carmel, 31905 Haifa, Israel

^b State Key Laboratory for Mineral Deposits Research, School of Earth Sciences and Engineering, Nanjing University, Nanjing, Jiangsu 210093, PR China

^c Department of Geological and Environmental Sciences, Ben-Gurion University in the Negev, Beer Sheva 84105, Israel

Received 26 September 2017; accepted in revised form 27 May 2018; available online 4 June 2018

Abstract

Magnesium isotopes in early diagenetic dolomite have been proposed as a potential tracer for seawater chemistry and global Mg cycles. However, the applicability of Mg isotopes of early diagenetic dolomite in studies of ancient seawater requires a detailed understanding of the behavior of Mg isotopes during dolomitization in a variety of geological settings. Hinterland attached carbonate platform is an important sink of seawater Mg through dolomitization, and basin restriction is a common feature in hinterland attached carbonate platforms, yet its effects on Mg isotope systematics in carbonates have not been well documented.

The upper Albian Hevyon Formation in southern Israel was deposited in a typical hinterland attached carbonate platform setting and provides an ideal case for investigating the Mg isotope behavior during dolomitization in environments of frequent basin restrictions. The abundance of dolomite increases up-section in the Hevyon Formation and correlates with the appearance of microbial deposits and disappearance of metazoans, reflecting water level fluctuations in multiple exposure and recharging events. In conjunction with sedimentary facies analysis, multiple geochemical proxies (Ni/Co, V/Cr, Ce/Ce*, and $\delta^{13}\text{C}$) indicate the development of anoxic conditions. These two lines of evidence, together with textural indicators and $^{87}\text{Sr}/^{86}\text{Sr}$ ratios, suggest dolomitization was microbial and penecontemporaneous in a shallow low circulation water body. $\delta^{26}\text{Mg}$ of dolomite increases from $-1.99 \pm 0.12\text{\textperthousand}$ in the lower part of the sequence to a value of $-1.52 \pm 0.02\text{\textperthousand}$ in the middle interval, then decreases back to $-2.06 \pm 0.18\text{\textperthousand}$ in the upper unit.

Overall, Mg isotope compositions co-vary with $\delta^{13}\text{C}$, Mg/Ca ratios, as well as crystal size of dolomite, which implies that variations in $\delta^{26}\text{Mg}$ value reflect syn-depositional changes in water chemistry as a result of dolomitization in episodically restricted basins. $\delta^{26}\text{Mg}$ tracks the fluctuating marine connection and provides a powerful tracer for the level of restriction. Furthermore, by pairing Mg isotope variability of the dolomite with a Rayleigh distillation model and elemental mass balance

* Corresponding authors.

E-mail addresses: obialik@campus.haifa.ac.il (O.M. Bialik), liweiqiang@nju.edu.cn (W. Li).

in aqueous solution, it is possible to constrain the Mg/Ca ratio of seawater. Based on the records from the Hevyon Formation, Mg/Ca ratio of seawater during the Albian is constrained between 1.5 and 1, which is consistent with results from other records.

© 2018 Elsevier Ltd. All rights reserved.

Keywords: Dolomite; Carbonate platforms; Seawater Mg/Ca ratio; Basin restriction; Mg isotopes; Levant

1. INTRODUCTION

Dolomitization is a major sink for Mg from seawater, and the secular changes in global dolomitization intensity have been proposed as the cause of long-term variations in Mg concentration and Mg/Ca ratio of seawater in geological history (Wilkinson and Algeo, 1989; Arvidson et al., 2011). Notably, the decrease in reef and platform carbonate production during the Cretaceous (Kiessling et al., 1999, 2003), and initiation pelagic carbonate deposition (Davies and Worsley, 1981; Hay et al., 1988) coincided with the diminishing fraction of dolomite in carbonate deposits since the Albian and the increase in seawater Mg/Ca ratios (Given and Wilkinson, 1987). This correlation implies the importance of dolomitization on carbonate platform in global Mg cycling.

Carbonate platforms can be divided into two categories: isolated platforms (such as the Great Bahamas Bank and the Maldives), and hinterland attached platforms (such as the Florida Platform). Hinterland attached carbonate platforms are notably greater in size and more abundant in low to intermediate continental shelves throughout the geological history (Kiessling et al., 2003). In addition, hinterland attached platforms hold a combination of environmental conditions favorable for dolomitization, such as the likelihood to basin restriction that leads to saline, stratified, low oxygen environments (Sass and Katz, 1982; Vahrenkamp and Swart, 1994; Warren, 2000; Machel, 2004; Meister, 2013). Therefore, hinterland attached platform plays an important role in global cycling of Mg.

Magnesium isotopes are an emerging tool to study carbonates (Teng, 2017), and significant Mg isotope fractionation occurs during precipitation of dolomite from aqueous solutions (Higgins and Schrag, 2010; Li et al., 2015). Stoichiometric dolomite is a robust archive of Mg isotope signature as it is less sensitive to post-depositional resetting (Geske et al., 2012; Li et al., 2016; Hu et al., 2017) compared to calcite (Rollion-Bard et al., 2016; Riechelmann et al., 2016; Mavromatis et al., 2017; Chanda and Fantle, 2017). In addition, it has been hypothesized that secular changes in dolomitization intensity may result in changes in Mg isotope compositions of seawater, which were in turn recorded in carbonate precipitates (Li et al., 2015). This hypothesis is based on a static Mg isotope mass balance principle for oceans and an assumption of adequate isotope exchange between dolomite and seawater during dolomitization (Tipper et al., 2006). However, it is unclear whether such assumption is satisfied in real dolomitizing systems that are usually complex (Warren, 2000). For example, Mg isotope variation in carbonate sediments can be explained by the evolution of $\delta^{26}\text{Mg}$ in pore fluids during

diffusion-transport-reaction of Mg ions during diagenesis (Higgins and Schrag, 2010; Fantle and Higgins, 2014; Mavromatis et al., 2014; Huang et al., 2015; Chanda and Fantle, 2017). Furthermore, on a larger scale, Mg isotope composition of water body in restricted basins may change due to progressive dolomitization, replenishment from seawater during high sea-level phases, and mixing with continental runoffs. These possibilities add complexities to the Mg isotope systematics and need to be assessed in interpretations of Mg isotope data from natural carbonates.

The Albian (113–100 Ma) witnessed widespread developments of large carbonate platforms and dolomitized marginal carbonates in North America (Fisher and Rodda, 1969), at both sides of the emerging South Atlantic (Koutsoukos et al., 1993), around the Pacific Ocean (Flood and Chivas, 1995) and the Tethys (Vlahović et al., 2005). These platforms grew in the aftermath of oceanic anoxic event 1b and the collapse of the Urgonian platform phase (Föllmi and Gainon, 2008). Their establishment took place during the retreat of the oxygen minimum zone back into a deeper position (Erbacher et al., 1999) and at the midst of the pCO₂ increase (Haworth et al., 2005). In this study, we investigated the sedimentology, petrography, mineralogy, major and trace elements, as well as isotope (C-O-Sr-Mg) compositions of the upper Albian Hevyon Formation in southern Israel that serve as an example of a hinterland attached large carbonate platform. By taking such integrated approach, we aim to elucidate the controlling factors of dolomitization in this specific sedimentary setting. Furthermore, the case of hinterland attached large carbonate platform provides an opportunity to test the response of Mg isotopes to dolomitization in a restricted setting and the applicability of Mg isotope geochemistry to problems in carbonate sedimentology.

2. GEOLOGICAL SETTING

During the Albian, the northern margin of the Arabian plate was situated near the equator (Fig. 1a), allowing the development of large carbonate platforms (Ziegler, 2001), which many exhibit an unconformity in the Late Albian due to the culmination of a transgressive phase (Scott, 1990; Alsharhan and Kendall, 1991; Masse et al., 1997). The long-term transgressional trend on the northern Arabian margin (Haq and Al-Qahtani, 2005) led to a transition from siliciclastic to calcareous depositional settings (Bialik and Waldmann, 2017), which was superimposed by second-order sea level changes that eventually led to episodic exposure events and deposition of siliciclastics on the platform (Sharland et al., 2001). The southern part of Israel and northern Sinai were re-flooded during the Aptian

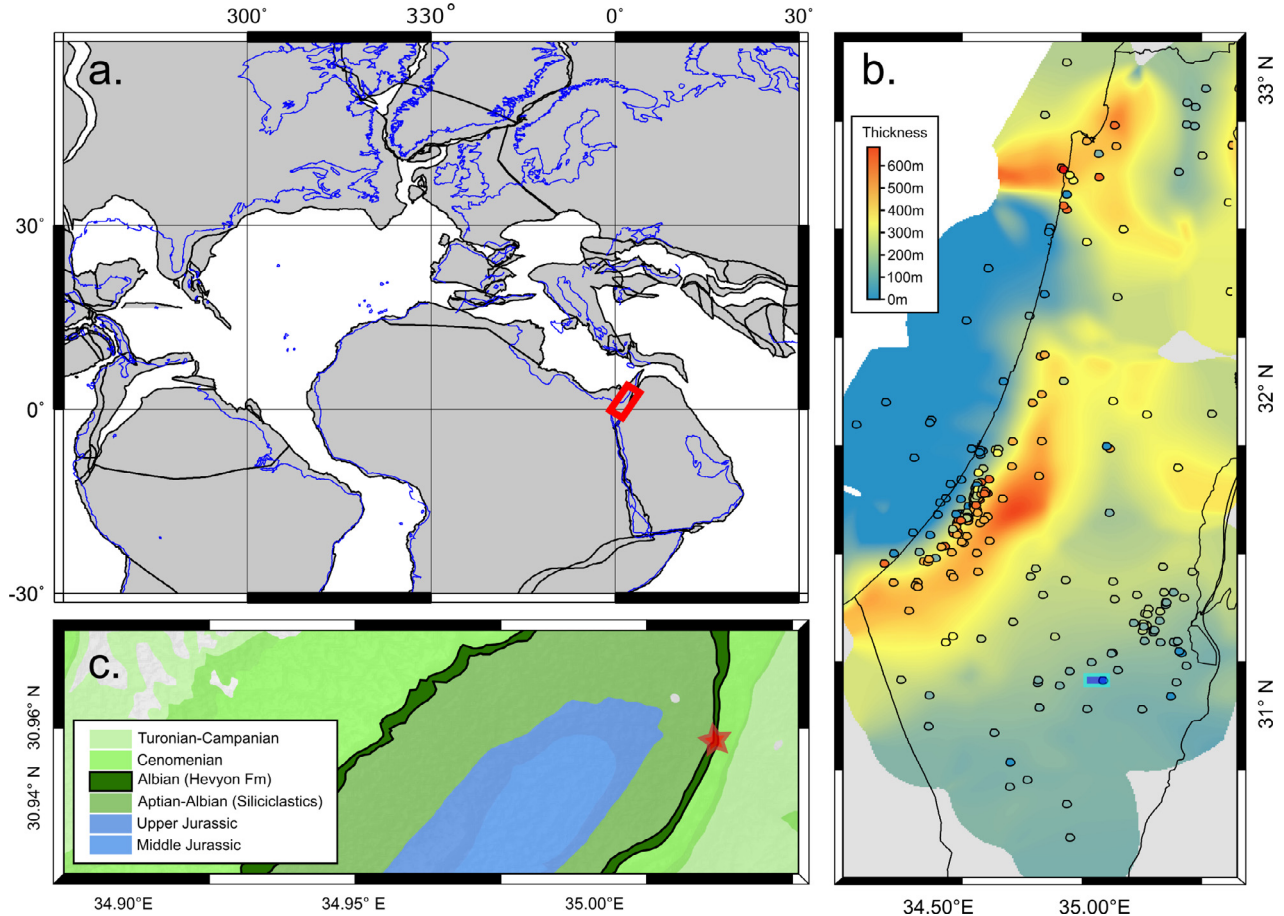


Fig. 1. Paleogeographic and geological settings of the studied dolomite section. (a) Paleogeographic reconstruction of the Late Albian (Hay et al., 1999), the red frame annotates the location of Fig. 1b. (b) Thickness distribution of the Hevyon/Yagur dolomitic lithosome in Israel. Circles annotate locations of individual drill cores or outcrops where thickness data is available; the blue rectangle denotes the area in Fig. 1c. (c) Geological map of Makhtesh Hatira, the location of the MG section is marked by the red star. (For interpretation of the references to color in this figure legend, the reader is referred to the web version of this article.)

depositing a calcareous unit in a restricted marine system (Jenkins et al., 1984; Braun and Hirsch, 1994). This sequence was overlain by distinct volcanic pyroclastic and basalt layers ca. 99 Ma ago (Segev and Sass, 2009).

The calcareous portion of the Albian sequence forms a single extensive lithosome in Israel named as the Yagur and Hevyon formations, in the northern and southern parts of the country, respectively. These dolostones, minor limestones and shales units were interpreted to characterize a large-scale carbonate platform (Hirsch and Braun, 1994) and inhabit a low latitude, arid to semi-arid warm climate (Ibrahim, 2003). The dolomitization pattern of the platform is irregular. While nearly all sites in Israel are dolomitized, the Hevyon in northern Sinai occurs as dolomitic and non-dolomitic with multiple rudist horizons representing shelf facies (Steuber and Bachmann, 2002).

The thickness of the Hevyon/Yagur lithosome ranges from a few tens of meters to over half a kilometer, with the maximum thickness occurring in the subsurface of the coastal plain of Israel (Fig. 1b). The lithosome greatly thins westwards and northwards, with a transition to peri-platform environment comprised primarily of calcarenite

and calcilutite with prevalent rudist debris (Talme Yafe Fm. sensu Bein and Weiler, 1976). The geometry of the lithosome in the subsurface of the coastal plain is clinoformal according to Gardosh et al. (2011), suggesting it represents the prograding edge of the platform.

The type section of the Hevyon Formation is located at Makhtesh Hatira (Fig. 1c) and has been described in detail by Lewy (1988), who constrained the age of the section to Albian based on occurrence of the ammonite *Hypengonoceras* in the unit, the first occurrence of *Praealveolina* and the earliest Cenomanian Ammonites in the topmost layer of the unit. Independent radiogenic dating of glauconite in this sequence corroborate the proposed chronology, although with limited accuracy due to contamination of secondary autogenic phases (Sandler and Harlavan, 2006).

3. MATERIAL AND METHODS

3.1. Site selection and sampling

The Hevyon Formation was systematically described and sampled on the southern side of Makhtesh Hatira. This

section (labeled MG, Fig. 1c) was selected because the maximum burial depth the section experienced was <1 km (Gvirtzman, 2004). Because the local thermal gradient is ~20 °C/km (Eppelbaum, 1996), burial metamorphism can be excluded, and only authigenic processes superimposed on this section. A total number of 212 samples were collected for this study, and thin sections were made from 93 of these samples, which were further described following Wright (1992) systematics.

3.2. Analytical methods

3.2.1. XRD and SEM

Crystal size distribution was measured (long axis, minimum 30 idiomorphic crystals per sample) from fragments and thin sections of selected samples using a Jeol NeoScope benchtop SEM. XRD analysis was carried out for bulk sample powders using a Rigaku MiniFlex 600 benchtop X-ray diffractometer (30 kV/10 mA from 3° to 70° at 0.05° increments by point detector) at the University of Haifa or a Rigaku Rapid II dual-source rotating anode X-ray diffractometer (40 kV/100 mA, 2-dimensional image plate detector) at Nanjing University, both running with a Cu target X-ray source. The relative abundance of dolomite and calcite in carbonate was estimated from the intensities of the (1 0 4) peaks (Zevin, 1979). Magnesium content in dolomite was calculated based on the dolomite (1 0 4) peak position (Goldsmith and Graf, 1958), Mg content in calcite was calculated using the empirical curve of Zhang et al. (2010), and the degree of order in dolomite was calculated following Graf and Goldsmith (1956).

3.2.2. Bulk rock chemistry

Major element compositions of the samples were analyzed using an X-ray fluorescence spectrometer (XRF) at ALS Chemex (Guangzhou). The analytical precision is 1–3% for elements with contents >1 wt% and is <5% for elements with contents <1 wt%. Trace element concentrations were determined by inductively coupled plasma-mass spectrometry (ICP-MS) at ALS Chemex (Guangzhou), with analytical precision of better than 5% for trace elements with concentrations >50 ppm, for trace elements with concentrations <50 ppm, the precision is better than 10%.

3.2.3. C-O isotopes

Carbon and oxygen isotope compositions of whole rock powder samples were measured using a Thermo Delta V GS-IRMS equipped with a Gas Bench II in the Environmental Stable Isotopes Laboratory at Ben-Gurion University of the Negev or a Thermo Delta Plus continuous flow IRMS at Nanjing University. Samples were reacted with 100% phosphoric acid at 70 °C and allowed to cool prior collection of CO₂ and measurements to ensure full digestion of the dolomite. The external precision of δ¹⁸O and δ¹³C measurements on both instruments is better than ±0.5‰.

3.2.4. Sr isotopes (⁸⁷Sr/⁸⁶Sr ratios)

Sr isotope analysis was performed following the procedure of Bailey et al. (2000). About 10 mg of the whole rock powder was reacted with 1 N ammonium acetate at

room temperature for over 3 days. Then the rock powder was dissolved in 1 N acetic acid after rinsing in deionized water for 3 times. The supernatant liquid of the dissolve sample was extracted, dried, re-dissolved in concentrated HNO₃ and dried. Treatment using concentrated HNO₃ was repeated, then the sample was dissolved in 1 mL 3 N HNO₃ and ready for ion exchange chromatography. Sr was purified using Sr-spec resin (De Muynck et al., 2009). USGS igneous reference material AGV-2 was processed as unknowns with the samples for quality control. Strontium isotope ratios were measured using a Thermo Scientific Triton TIMS at Nanjing University (Hu et al., 2017). ⁸⁷Sr/⁸⁶Sr ratios were normalized to ⁸⁶Sr/⁸⁸Sr = 0.1194 using exponential law during each analysis. Pure strontium reference NIST 987 was analyzed at the beginning of every analytical sequence. The measured ⁸⁷Sr/⁸⁶Sr ratios of the geological and pure metal reference materials are in agreement with published values (Hu et al., 2017).

3.2.5. Mg isotopes

For Mg isotope analysis, about 50 mg rock powder was dissolved in concentrated nitric acid, and an aliquot of the dissolved carbonate sample solution that contained 50 µg Mg was used for ion exchange chromatography. Magnesium in this aliquot was separated from matrix elements using a two-stage ion exchange procedure that has been reported in detail by Hu et al. (2017). Mg recovery of the two-stage column chemistry was >95%, and matrix elements were <1% of Mg after purification. Measurement of Mg isotope ratios was performed on a Thermo Fisher Scientific Neptune Plus MC-ICP-MS at Nanjing University. The instrument was running at low-mass-resolution and wet plasma mode, using a 100 µL/min concentric self-aspirating nebulizer. A 40 s on-peak acid blank was measured before each analysis. Each Mg isotope ratio measurement consisted of fifty 4-s integrations, and the typical internal precision (2 standard error or 2SE) was better than ±0.04‰ for ²⁶Mg/²⁴Mg and ±0.02‰ for ²⁵Mg/²⁴Mg. The long-term external reproducibility (2 standard deviations or 2SD) of Mg isotope analysis is better than ±0.10‰ in ²⁶Mg/²⁴Mg and ±0.05‰ in ²⁵Mg/²⁴Mg, based on repeat analyses of multiple Mg isotope standard solutions against in-house stock solutions (Appendix Table S1). All samples and standards were concentration matched to minimize instrumental bias (Teng and Yang, 2014).

Magnesium isotope data were reported relative to the international Mg isotope standard (DSM3) using conventional δ notation to express per thousand deviations from DSM3:

$$\delta^{2x}\text{Mg} = \left(\frac{{}^{2x}\text{Mg}/{}^{24}\text{Mg}_{\text{sample}} - {}^{2x}\text{Mg}/{}^{24}\text{Mg}_{\text{DSM3}}}{{}^{2x}\text{Mg}/{}^{24}\text{Mg}_{\text{DSM3}}} \right) \times 1000$$

where x = 5 or 6.

A pure in-house Mg standard solution from High Purity Standards Company (Lot No. HPS909104) was used as the bracketing standard for Mg isotope analysis by standard-sample-standard bracketing routine. The concentration of samples typically matched the standard solution at 1 ± 0.1 ppm. The Mg isotope composition of HPS909104 Mg in-house standard relative to international standard DSM3 has been well characterized using two

different (IsoProbe and Nu Plasma II) MC-ICP-MS at University of Wisconsin - Madison for over 5 years ($\delta^{26}\text{Mg} = -0.66\text{\textperthousand}$ relative to DSM3, Li et al., 2011, 2012, 2014, 2015) and additionally certified using a third (Nep tune plus) MC-ICP-MS at Nanjing University for over 1 year ($\delta^{26}\text{Mg} = -0.67\text{\textperthousand}$ relative to DSM3, Hu et al., 2017).

The accuracy of Mg isotope measurements was verified by measured $\delta^{26}\text{Mg}$ values for Cambridge1, a second international Mg isotope standard, which is $-2.59 \pm 0.07\text{\textperthousand}$ (2SD, n = 16), consistent with published values (e.g., $-2.58 \pm 0.14\text{\textperthousand}$, Galy et al., 2003; $-2.57 \pm 0.12\text{\textperthousand}$, Li et al., 2012; $-2.63 \pm 0.03\text{\textperthousand}$, Teng et al., 2015; $-2.58 \pm 0.07\text{\textperthousand}$, Chanda and Fantle, 2017). The accuracy of the total procedure was verified by analyses of IAPSO seawater standard and three USGS rock standards (BHVO, DST-2, BIR) that were processed as unknowns along with samples by column chemistry. The measured $\delta^{26}\text{Mg}$ values of the seawater and rock standards matched the published values in literature within $\pm 0.10\text{\textperthousand}$, and mostly within $\pm 0.05\text{\textperthousand}$ (Appendix Table S1).

4. RESULTS

4.1. Sedimentological description

The Hevyon Formation as exposed in Makhtesh Hatira has a thickness of 113.2 m and is comprised of alternating limestone, dolostone and marl (Fig. 2). The calcareous lithologies of the Hevyon Formation show vertical heterogeneity, with the lower half (up to 49 m) of the unit predominantly calcitic and the upper half predominantly dolomitic (both dolostone and marl), with the exception of the uppermost 8 m that consists of calcite-rich units. Silty layers within the section are mostly lithified, contrary to the compacted and poorly lithified marly beds.

The calcitic lower half of the Hevyon Formation is punctuated by 0.2–1.5 m thick dolomitic beds and 0.3–1 m thick marly beds. At least nine of these beds form a gradual transition series from marl to calcareous lithology and a sharp transition back to marl (Fig. 3a). This portion of the unit host multiple fossiliferous beds, containing bivalves (including rudist, in living and nonliving orientations (Fig. 3b), echinoderm plates (Fig. 1Sa), gastropods (Fig. 1Sb) and rare ammonites. Bioturbation varies from fully bioturbated to completely absent in intervals of fine lamination (Fig. 3c and 1Sc). Sedimentary textures range from mudstone to rudstone, with the most common form being mudstone, wackestone, and packstone (in descending order). Fossils become scarce above the base of the unit from 33 m, and mudstone and wackestone become the dominant phases until the transition to the more dolomitic upper half of the unit. Glauconite is found at the base of the unit as a minor component in some of the detrital rich layers (Fig. 1Sd). There is abundant visible porosity in this interval, primarily moldic porosity, between 16 m and 22 m above the base of the unit there is an interval that also hosts vuggy porosity and sparry cement in both types of porosity.

At the interval between 49 m and 103.5 m, dolomite becomes the dominant carbonate mineral, and the lithology

of this part of unit alternates between dolostone and dolomitic marl, with two horizons of flint occurring at 57 m and 98 m. Sediment layer thickness ranges between 0.1 m and 4.7 m for dolostones, and between 0.1 m and 1.9 m for dolomitic marls. The thickness distribution of the marl does not exhibit a clear pattern, whereas thicker dolostones mainly occur at above 70 m. Very few metazoan fossils were preserved in this part of the unit, except for small gastropods. Microbialites are common between 60 m and 105 m, mainly tabular flat laminate, undulatory to pseudocolumnar in forms (Fig. 3d). When visible, the principal identified texture point to mudstone, followed by microbialitic boundstone, with seven sparstone intervals between 55 m and 80 m (Fig. 1Se).

Desiccation cracks were encountered from 56 m to 58 m (Fig. 3e), where *Microcodium* was found. Another set of desiccation cracks was encountered at 66.4 m above the base of the unit. Porosity in this interval is primarily vuggy, followed by fenestral (Fig. 1Sf). Moldic porosity is also present, sparry cement fill occurs in the vuggy and moldic pores, but most of the fenestral porosity is open. Most of the porosity is concentrated between 52 m and 80 m and can be divided into three principle intervals of 52–58 m, 62–66.4 m and 73–80 m; the first two coincide with the occurrence of desiccation cracks. The co-occurrence of the diagenetic features and subaerial textures such as desiccation cracks implies these high porosity phases are related to syngenic exposure events.

Above 103.5 m until the top of the unit, limestone becomes dominant and dolomitic content sharply declines, and while there are silty layers, marl is not present. Metazoan macrofossils including gastropods and bivalves reappear in this interval, with the top of the unit capped by a layer dominated by the bivalve *Pycnodonte vesiculosus* (Fig. 3f). Wackestone and packstone become more abundant as well as grainstone in the top layer.

4.2. Mineralogy

Based on XRD analyses, three principal groups of dolomite stoichiometry are distinguished: Ca-dolomite ($\text{Ca}_{1.03-1.05}\text{Mg}_{0.95-0.97}(\text{CO}_3)_2$), near stoichiometric dolomite ($\text{Mg}_{1-1.04}\text{Ca}_{0.96-1}(\text{CO}_3)_2$) and Mg-dolomite ($\text{Mg}_{1.06}\text{Ca}_{0.94}(\text{CO}_3)_2$) (Appendix Table S2). Ca-dolomite is more common in the lower half of the unit whereas near stoichiometric, and Mg-dolomite is more common in the upper half, except for the interval above 103 m that hosts only Ca-dolomite (Fig. 2). There are two groups of calcite stoichiometry: low Mg calcite I ($\text{Ca}_{0.95-0.94}\text{Mg}_{0.05-0.06}\text{CO}_3$) and low Mg calcite II ($\text{Ca}_{0.98-0.97}\text{Mg}_{0.02-0.03}\text{CO}_3$). All limestones in the lower half of the unit (until 56 m) are comprised of low Mg calcite II, whereas limestones in the upper half unit contain higher Mg (low Mg calcite I).

SEM analyses revealed that the dolomite crystals are predominantly euhedral, with crystal size between 3 μm to over 100 μm (Fig. 1Sg and 1Sf). There is no obvious correlation between crystal size and stoichiometry of the dolomite (Fig. 4), although the scattering of crystal size distribution increases from Mg-dolomite (from $4.0 \pm 4.1 \mu\text{m}$ to $14.7 \pm 6.4 \mu\text{m}$, average $8.4 \pm 3.3 \mu\text{m}$) to near stoichiometric

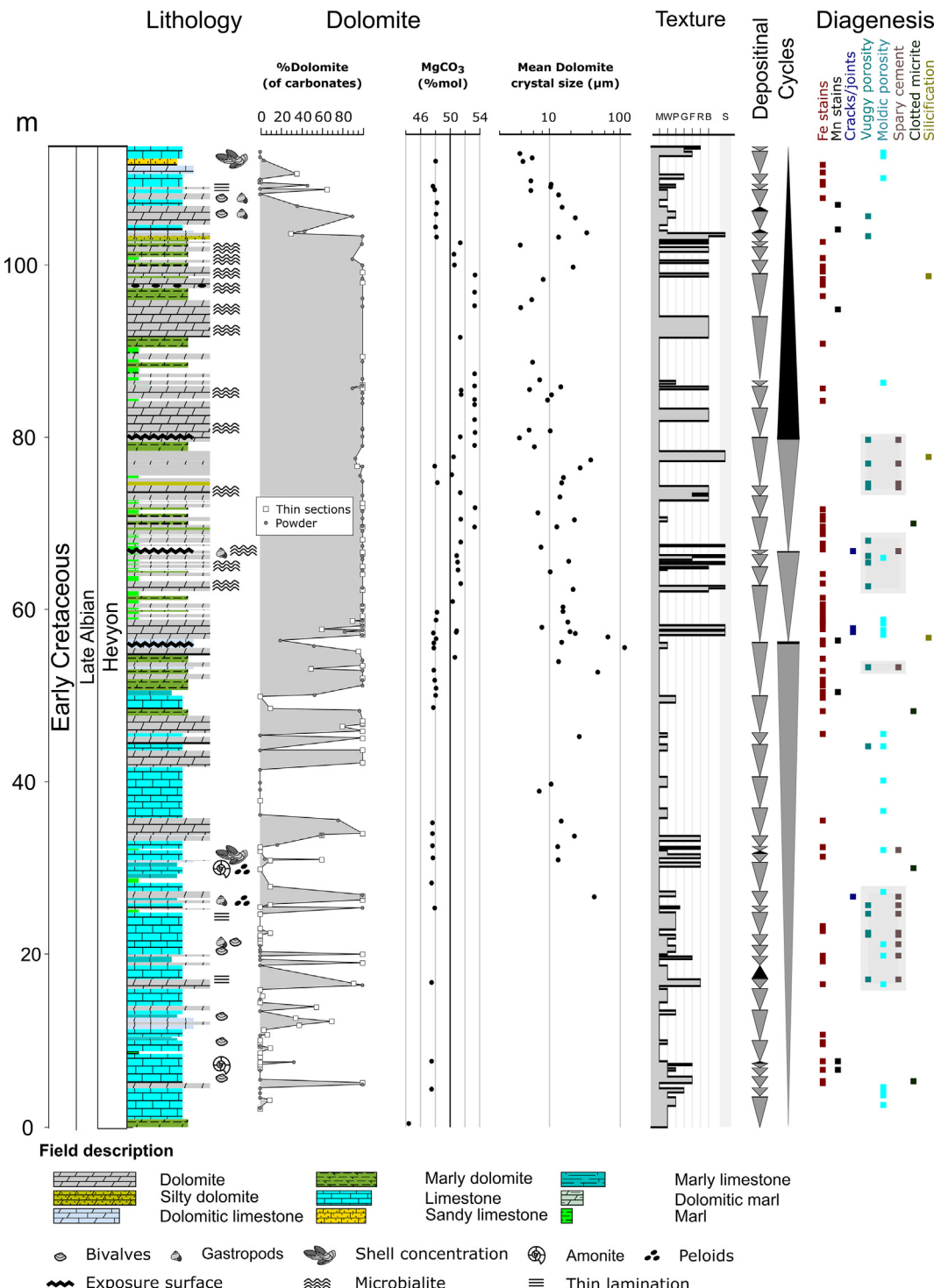


Fig. 2. Columnar section of the Albion Hevyon Formation in Makhtesh Hatira, showing: lithology, sedimentary field and petrographic findings; dolomite fraction of carbonates (gray point – XRD powder diffraction, white squares – thin section XRD), dolomite stoichiometry and crystal sizes; sedimentary textures (M – mudstone; W – wackestone; P – packstone; G – grainstone; F – floatstone; R – rudstone; B – boundstone; S – sparstone) and diagenetic features.

dolomite (from $3.9 \pm 1.5 \mu\text{m}$ to $38.9 \pm 7.0 \mu\text{m}$, average $14.5 \pm 8.9 \mu\text{m}$), to Ca-dolomite (from $4.3 \pm 5.8 \mu\text{m}$ to $115.9 \pm 20.1 \mu\text{m}$, average $26.8 \pm 25.5 \mu\text{m}$). Detailed SEM

analyses further revealed halite embedded within dolomite crystals (Fig. 1Si and 1Sj), and residual organic matter attached to dolomite crystals (Fig. 1Sk and l).

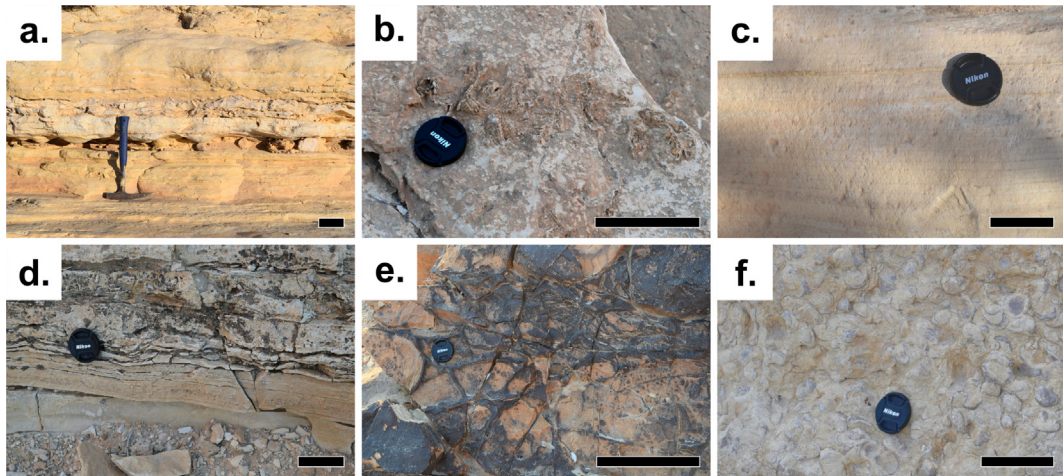


Fig. 3. Mesoscale sedimentary features of the Albian Hevyon Formation in Makhtesh Hatira, south Israel. (a) Marl/limestone alternations in the lower part of the Hevyon Formation, note the fine lamination in the marl (yellow) beds; (b) Rudists in the lower half of the Hevyon Formation (center photo); (c) Fine laminations in the lower half of the Hevyon Formation; (d) Laminated microbialites in the dolomitic middle portions of the Hevyon Formation; (e) Desiccation cracks highlighted by silicification; (f) The Pycnodonte vesiculosus bed at the top of the Hevyon Formation. Scale bar in all photos is 10 cm. (For interpretation of the references to color in this figure legend, the reader is referred to the web version of this article.)

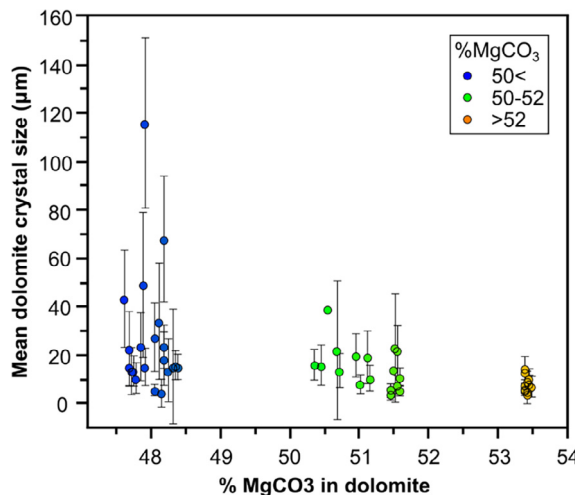


Fig. 4. Plot of dolomite stoichiometry versus crystal size. Three distinct groups of dolomite stoichiometry can be identified, and Ca-dolomite ($\text{Ca}_{1.03-1.05}\text{Mg}_{0.95-0.97}(\text{CO}_3)_2$) exhibits the largest range of crystal size, whereas near stoichiometric dolomite ($\text{Mg}_{1.04}\text{Ca}_{0.96-1}(\text{CO}_3)_2$) and Mg-dolomite ($\text{Mg}_{1.06}\text{Ca}_{0.94}(\text{CO}_3)_2$) have a smaller range of crystal size.

4.3. Bulk rock chemistry

The bulk rock chemistry of the Hevyon Formation varies stratigraphically (Fig. 5a and b, Appendix S2), exhibiting different behaviors in the lower and upper limestone portions relative to the middle dolostone interval. Bulk rock Sr contents (Fig. 5) range between 177 and 505 ppm in calcite dominant rocks and between 108 and 355 ppm in dolomite dominant rocks, decreasing continuously from the base of the unit to a minimum value at 71 m and increasing up-section.

Manganese content (Fig. 5) ranges from 138 to 878 ppm in limestones and from 168 to 1311 ppm in dolostones, except for one sample with Mn content of 2267 ppm at the base of the unit. The sample with anomalously high Mn content has visible Mn stains in hand specimen and thin sections. There is a general trend of diminishing Mn baseline from ~500 ppm at the base of the unit to ~160 ppm at the top of the unit. Superimposed on this trend are several increases in Mn content, the largest of which occurs between 40 m and 80 m, its maximum at 60 m with values between 874 ppm and 1311 ppm. Another very sharp increase occurs between 101 m and 107 m, where Mn content increases from 197 to 1077 ppm before dropping to 138 ppm at 108 m.

Ni/Co ratios range from 3 to >200, while V/Cr ranges from 0.7 to 5.6. Ni/Co ratio is above 8 in most of the unit, with the lowest level occurring between 46 m and 105 m, whereas V/Cr ratio is below 2 in most of the unit, with high values mainly occurring between 58 m and 98 m. Ce/Ce* ranges from 0.12 to 1.57, which is notably high between 0 m and 35 m and between 48 m and 96 m, ranging from 0.89 to 1.57 (mean 1.33 ± 0.13 n = 25), and from 0.39 to 1.53 (mean 1.20 ± 0.25 n = 45), respectively.

4.4. Isotopic compositions

Isotopic compositions of carbon, oxygen, magnesium and strontium are variable in the Hevyon Formation (Fig. 6, Appendix Table S2). Both $\delta^{18}\text{O}$ and $\delta^{13}\text{C}$ values exhibit large variability within the Hevyon Formation, that $\delta^{18}\text{O}$ ranges from $-7.8\text{\textperthousand}$ to $4.5\text{\textperthousand}$ (mean = $1.6 \pm 2.3\text{\textperthousand}$, n = 157) and $\delta^{13}\text{C}$ from $-5.3\text{\textperthousand}$ to $3.1\text{\textperthousand}$ (mean = $0.8 \pm 1.4\text{\textperthousand}$, n = 157). The majority of dolostones have a tight distribution of $\delta^{18}\text{O}$ values ($-2.1\text{\textperthousand}$ to $1.7\text{\textperthousand}$, mean = $-0.1 \pm 1.0\text{\textperthousand}$, n = 44), except for three samples that have higher values up to $4.5\text{\textperthousand}$ (mean = $3.8 \pm 0.5\text{\textperthousand}$, n = 3),

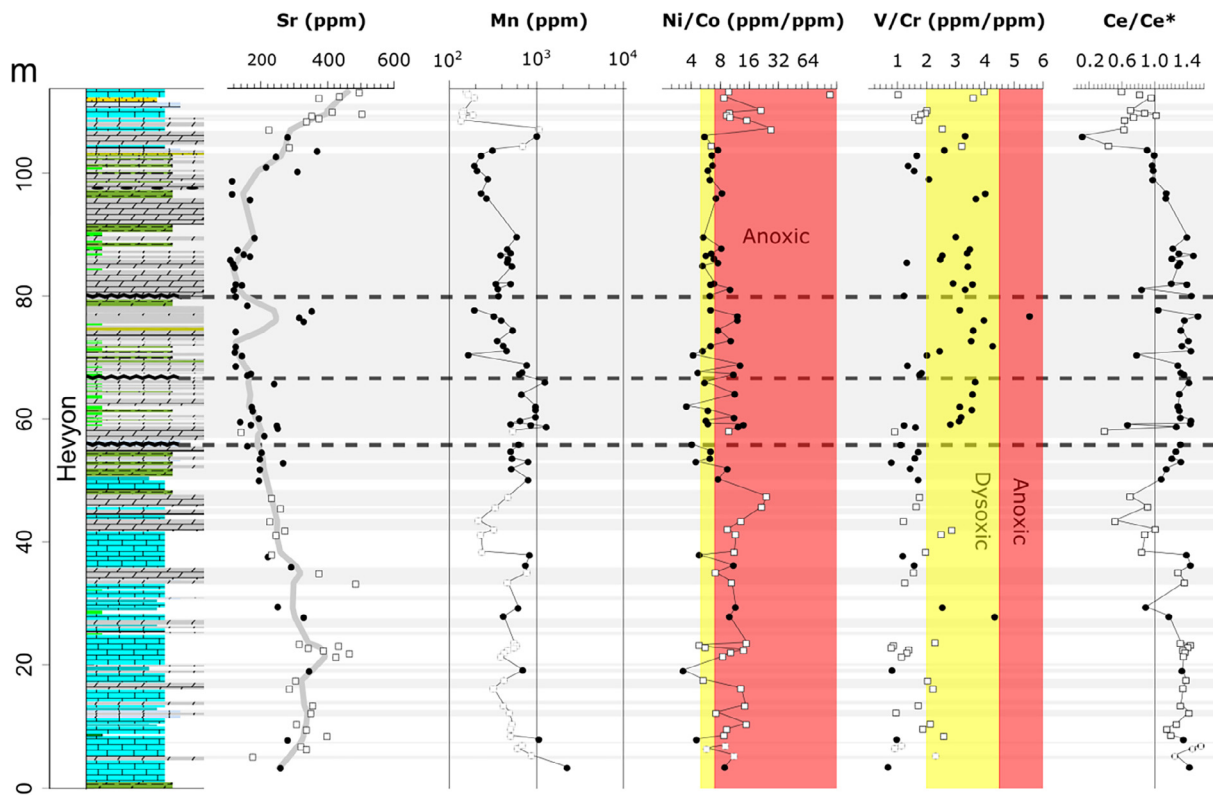


Fig. 5. Stratigraphic variations in bulk rock chemistry in the Heyyon Formation at Makhtesh Hatira for Sr and Mn concentrations, and ratios of Ni/Co, V/Cr, and Ce/Ce*. Squares represent limestone, and filled circles represent dolomite, grey horizontal bands indicate dolomitic domains. Colored vertical bands in the Ni/Co and V/Cr ratio plots show the ranges attributed to dysoxia and anoxia (Jones and Manning, 1994).

whereas $\delta^{18}\text{O}$ of limestones show in two distinct groups of $-8\text{\textperthousand}$ to $-4\text{\textperthousand}$ (mean = $-6.4 \pm 0.9\text{\textperthousand}$, n = 18) and $-2.5\text{\textperthousand}$ to 1\textperthousand (mean = $-0.6 \pm 0.8\text{\textperthousand}$, n = 12). On the contrary, limestones exhibit smaller variations in $\delta^{13}\text{C}$ values ($-1.4\text{\textperthousand}$ to $0.6\text{\textperthousand}$, mean = $0.4 \pm 0.8\text{\textperthousand}$, n = 30) than dolostones (see above). There is no clear correlation between $\delta^{18}\text{O}$ and $\delta^{13}\text{C}$ for samples from the section (Fig. 7a), although $\delta^{18}\text{O}$ and $\delta^{13}\text{C}$ of samples are negatively correlated in several specific intervals (e.g. 18–24 m, 62–70 m) but are positively correlated in other intervals (e.g. 30–50 m). There is no clear correlation between $\delta^{18}\text{O}$ or $\delta^{13}\text{C}$ and relative dolomite abundance in bulk rocks (Fig. 7b and c).

Except for one low value of $-2.30 \pm 0.09\text{\textperthousand}$ at the base of the unit, $\delta^{26}\text{Mg}$ values of dolostones remain relatively constant between the 4 m and 56 m with a mean value of $-1.99 \pm 0.12\text{\textperthousand}$ (n = 10). Between 56 m and 85 m, $\delta^{26}\text{Mg}$ values rise to a maximum of $-1.52 \pm 0.02\text{\textperthousand}$ with fluctuations, then decrease upsection. There is no correlation between $\delta^{18}\text{O}$ and $\delta^{26}\text{Mg}$ of dolostones, whereas $\delta^{13}\text{C}$ is positively correlated with $\delta^{26}\text{Mg}$ when $\delta^{13}\text{C}$ is below $0.8\text{\textperthousand}$, but negatively correlated with $\delta^{26}\text{Mg}$ when $\delta^{13}\text{C}$ is above $0.8\text{\textperthousand}$ (Fig. 8). It should also be noted that $\delta^{26}\text{Mg}$ is correlated with dolomite stoichiometry, which Ca-dolomite tends to have lower $\delta^{26}\text{Mg}$ values whereas Mg-dolomite tends to have higher $\delta^{26}\text{Mg}$ values, although near stoichiometric dolomite samples have a wide distribution of $\delta^{26}\text{Mg}$ values (Fig. 9).

$^{87}\text{Sr}/^{86}\text{Sr}$ ratios of the Heyyon Formation range between 0.707324 ± 0.000005 and 0.707890 ± 0.000004 , averaging at 0.707479 ± 0.000106 (n = 84). Dolostones have a small variation in $^{87}\text{Sr}/^{86}\text{Sr}$ ratios that range from 0.707324 ± 0.000004 to 0.707588 ± 0.000005 with a mean of 0.707414 ± 0.000040 (n = 47); limestones exhibit a wider $^{87}\text{Sr}/^{86}\text{Sr}$ range from 0.707890 ± 0.000004 to 0.707445 ± 0.0000047 with a mean of 0.707551 ± 0.000095 (n = 28). There is no clear stratigraphic trend of $^{87}\text{Sr}/^{86}\text{Sr}$ ratios other than the subdivision according to mineralogy (Fig. 6).

5. INTERPRETATION AND DISCUSSION

A significant Mg isotope variation is observed in the dolomite samples examined in this study. Such degree of variation in Mg isotope is typical in other dolomitic sequences as previously reported in literature (Jacobson et al., 2010; Fante and Higgins, 2014; Mavromatis et al., 2014; Husson et al., 2015; Huang et al., 2015; Peng et al., 2016). Interpretation of such isotopic variability requires knowledge of some fundamental sedimentary and diagenetic processes recorded in the dolomite, including the source of Mg, the timing and pathway of dolomite formation, and the depositional settings. Discussions on Mg isotope geochemistry of the dolomite, therefore, are preceded with necessary discussions on these sedimentary features in the Heyyon Formation based on integrated field and

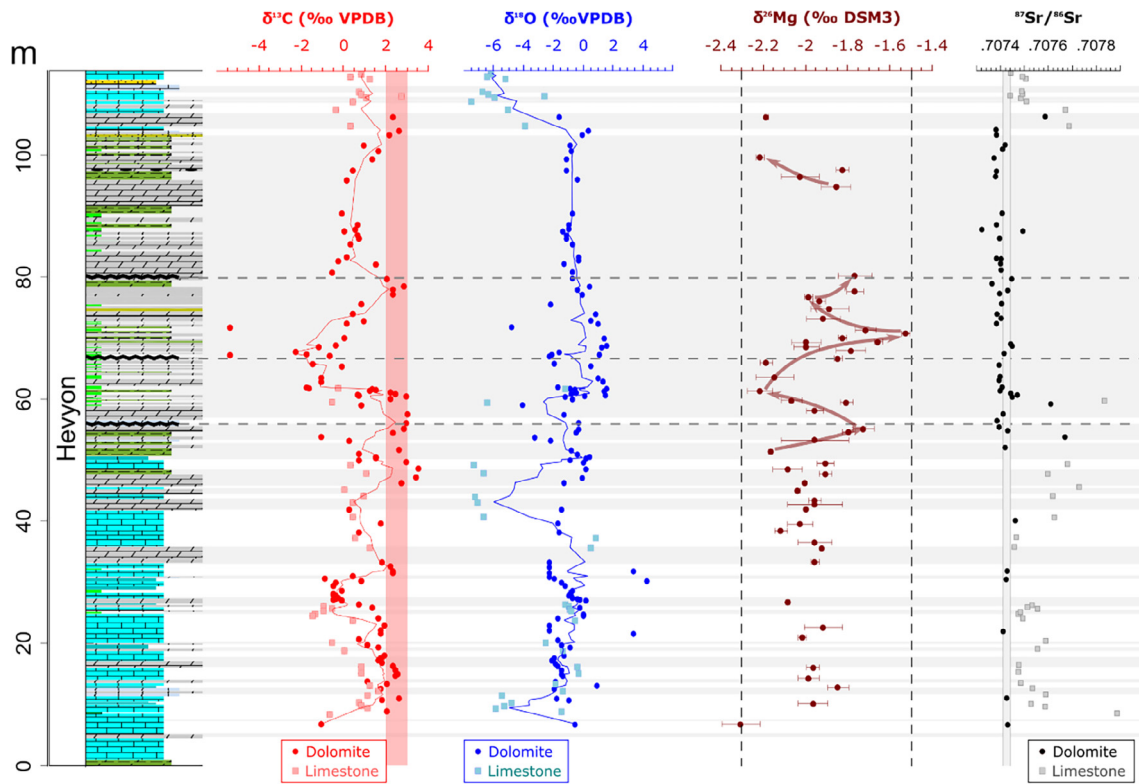


Fig. 6. Stratigraphic variations in bulk rock $\delta^{13}\text{C}$, $\delta^{18}\text{O}$, $\delta^{26}\text{Mg}$ and $^{87}\text{Sr}/^{86}\text{Sr}$ for carbonates in the Hevyon Formation at Makhtesh Hatira. The vertical pink band in $\delta^{18}\text{O}$ plot marks coeval marine values (Katz et al., 2005); arrows in the $\delta^{26}\text{Mg}$ plot mark the principle trends; the vertical gray band in $^{87}\text{Sr}/^{86}\text{Sr}$ plot indicates coeval seawater value (McArthur et al., 2001). Squares represent limestone and filled circles represent dolomite; gray horizontal bands indicate dolomitic domains. (For interpretation of the references to color in this figure legend, the reader is referred to the web version of this article.)

microscopic observations, mineralogical, elemental and C-O-Sr isotopic analyses.

5.1. Depositional settings

Based on the fossil assemblage and microfacies, the Hevyon Formation can be divided into three principle depositional regimes: open to restricted marine interval (0–49 m), restricted to exposure (49–103.5 m) interval and rapidly flooding interval (103.5 m until 113.2 m).

The first interval is characterized by abundant fossils including echinoderms and ammonites, which indicate open marine conditions and normal seawater salinity (Flügel, 2010). Oscillations in depositional textures, as well as variation in relative abundance of marl and dolomite in this interval, suggest alternations in the depositional setting. One notable feature in this interval is the occurrence of vuggy porosity between 16 m and 22 m, which indicates non-fabric selective dissolution by under-saturated solution, or by volume reduction during dolomitization (Ahr, 2008). Clear indications of exposure are absent in this interval, although there is an increase in abundance of packstones, suggesting a period of shallowing.

The transition from the first to the second interval is accompanied by the disappearance of macrofauna and an increase in thickness of the dolomite and marl beds,

as well as an increase in abundance of mudstones. The appearance of marl indicates either an increase in detritus supply or a regression to a position closer to the source of clasts. This, in conjunction with the desiccation cracks (exposure indicators) found between 56 m and 58 m and the occurrence of *Microcodium*, suggests a regression trend governed the shift from the lower to the middle interval. The occurrence of mudstones suggests low energy condition (Flügel, 2010), and when combined with the occurrence of microbialites, indicates restriction. The above exposure indicators point to at least three exposure events (Fig. 2), suggesting oscillations in accommodation space and energy, and imply that the basin was not entirely restricted but would have been episodically reconnected to the open ocean.

The third interval at the top of the unit records the disappearance of microbialites, reoccurrence of macrofauna as well as the return to limestone and a significant drop in siliciclastic abundance, all of which points to a transgressive trend and reduction in restriction. The *Pycnodonte vesiculosus* bed at the top of the unit marks a regional unconformity (Braun and Hirsch, 1994), capped further to the north with submerged submarine volcanic rocks (Segev and Sass, 2009). The lack of exposure features and the marine assemblage indicate that this unconformity marks a drowning event.

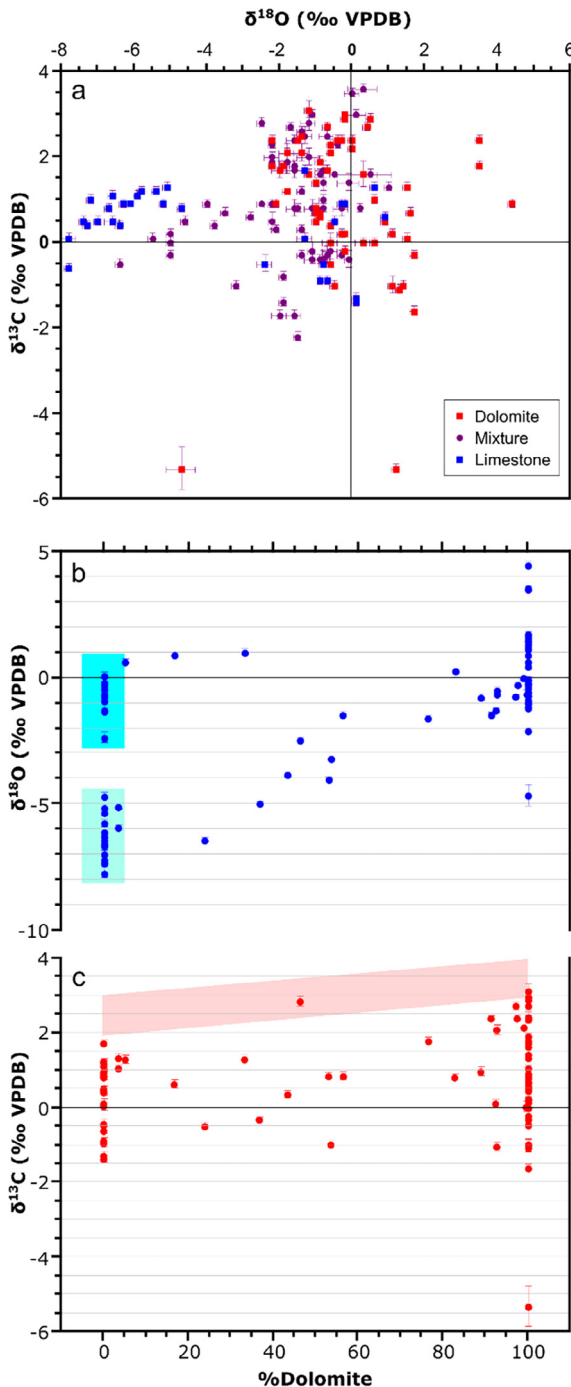


Fig. 7. Plots of C and O isotope data for the carbonates in the Hevyon Formation. (a) Crossplot of $\delta^{18}\text{O}$ versus $\delta^{13}\text{C}$, dolomite and limestone are marked as red and blue squares, respectively. (b) Crossplot of $\delta^{18}\text{O}$ versus dolomite content, calcite-rich samples cluster in two distinct groups, highlighted by the rectangles shades. (c) Crossplot of $\delta^{13}\text{C}$ versus dolomite content, the pink bar indicates the expected coeval marine $\delta^{13}\text{C}$ signature for dolomite-calcite mixture based on the limestone $\delta^{13}\text{C}$ curve by Katz et al. (2005) and the inter-mineral C isotope fractionation factors from Horita (2014), note that most measured values fall below the marine array. (For interpretation of the references to color in this figure legend, the reader is referred to the web version of this article.)

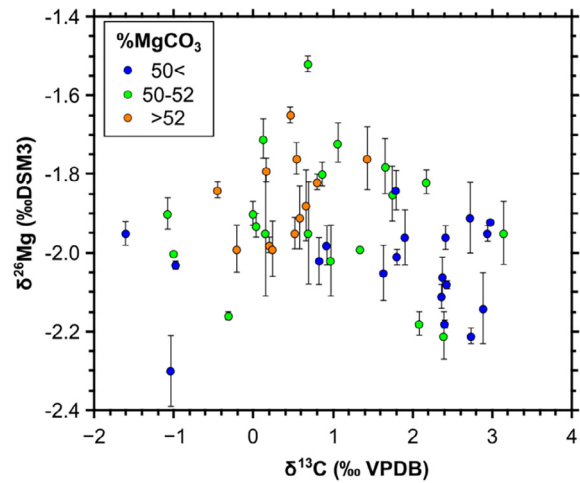


Fig. 8. Cross plot of $\delta^{26}\text{Mg}$ versus $\delta^{13}\text{C}$ for dolomite with different stoichiometry (see Fig. 4).

Overall, the depositional regimes were distinct in dolomitization intensity, and dolomite is the dominant carbonate mineralogy in the second interval of the section (Fig. 2) that contains clear sedimentary signatures of basin restriction. This implies a genetic connection between basin restriction and dolomitization of the section in this study.

5.2. Timing of dolomitization

Based on sedimentary facies analysis above, dolomitization in the Hevyon Formation was syndepositional. The interpretation of syndepositional dolomitization is further supported by petrographic evidence including (1) preservation of fine sedimentary textures in dolostones; (2) the lack of lithification in the marly layer, which indicates dolomite crystals should have grown within the sediment rather than cemented it; (3) the lack of brecciated dolomitization; and (4) the minimal cementation of open pores, which indicates that dolomitization was not dependent on available space and that dolomitization could provide the necessary rigidity to protect these pores from significant compaction.

Sr isotope chemostratigraphy is a useful tool to constrain the age of marine carbonates as seawater $^{87}\text{Sr}/^{86}\text{Sr}$ ratio varied in geological history (Veizer et al., 1999; McArthur et al., 2001). Despite its hinterland attached setting, the voluminous dolomite from the Hevyon Formation required massive Mg supply, which can only be provided by the seawater directly or indirectly. Therefore, seawater should be a major source of cations for the Hevyon Formation and the $^{87}\text{Sr}/^{86}\text{Sr}$ ratios of the carbonate are applicable for correlative comparison with the global seawater $^{87}\text{Sr}/^{86}\text{Sr}$ ratio curve in geological history. The $^{87}\text{Sr}/^{86}\text{Sr}$ ratios of carbonates in the Hevyon Formation display notable variations but overall, overlap with the stratigraphic coeval seawater value of 0.707414–0.707432 (McArthur et al., 2001). For limestone, the divergence from marine $^{87}\text{Sr}/^{86}\text{Sr}$ ratios increases with decreasing Sr concentration (Fig. 10a). However, nearly

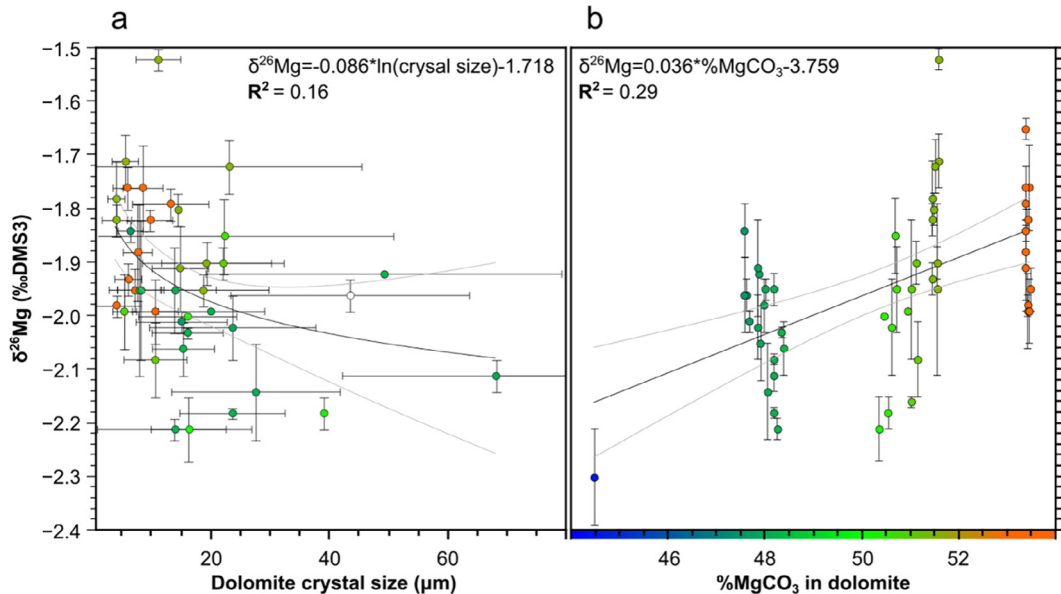


Fig. 9. Relation between Mg isotope compositions and mineralogical parameters of dolomite. (a) Cross plot of $\delta^{26}\text{Mg}$ versus dolomite crystal size. (b) Cross plot of $\delta^{26}\text{Mg}$ versus % MgCO_3 in dolomite. Point color in both plots represents % of MgCO_3 , with color scale on the x-axis of (b).

all dolomite samples have marine or near marine $^{87}\text{Sr}/^{86}\text{Sr}$ ratios for the Albian age.

Post-depositional overprinting is one of the contributors to the scattering in $^{87}\text{Sr}/^{86}\text{Sr}$ ratios. Based on $\delta^{18}\text{O}$ values, calcite-rich limestone samples from the section can be divided into two groups (Figs. 7 and 10b). A group of limestone with high (near marine) $\delta^{18}\text{O}$ values ($-2\text{\textperthousand}$ to $-4\text{\textperthousand}$) exhibit a tight $^{87}\text{Sr}/^{86}\text{Sr}$ ratio range of 0.70750 ± 0.00004 ($n = 14$). The second group of limestones have distinctly low ($-8\text{\textperthousand}$ to $-4\text{\textperthousand}$) $\delta^{18}\text{O}$ values, indicative of overprinting with meteoric water (Sharp, 2007), and exhibit an $^{87}\text{Sr}/^{86}\text{Sr}$ range of 0.70760 ± 0.00012 (Fig. 10c) that is distinct from the coeval seawater value. The combination of O and Sr isotope data, therefore, allows distinction between near pristine limestone and limestone that have been overprinted by late-stage fluids or formed under more estuarine conditions. Dolostones $\delta^{18}\text{O}$ values range from $-4.0\text{\textperthousand}$ to $4.5\text{\textperthousand}$ with the majority clustering around 0\textperthousand , which reflects insignificant meteoric water overprinting, supporting the greater robustness of dolomite against alteration than calcite (Hu et al., 2017).

The timing of the dolomitization is therefore constrained as contemporaneous with deposition based on combined geological and $^{87}\text{Sr}/^{86}\text{Sr}$ evidence (Fig. 10c). The key implication is that Mg in dolostones of the Hevyon Formation originated mainly from contemporaneous seawater, rather than post-depositional seawater/brine or continental riverine runoffs.

5.3. Mechanism of dolomitization

The occurrence of fine laminations in the sediment and the lack of bioturbation imply either poorly oxygenated conditions near the seafloor (MacEachern et al., 2010), or

a high salinity condition that was above the tolerance limit of bioturbating organisms, although the latter is usually represented by low diversity and abundance rather than total absence of bioturbation (Rodríguez-Aranda and Calvo, 1998; Jaglarz and Uchman, 2010). Additional evidence for low oxygen conditions includes the bulk rock chemistry, notably the elevated levels of Mn, Ce/Ce*, V/Cr and Ni/Co (Fig. 5b).

Mn is reduced from Mn^{4+} to Mn^{2+} and becomes mobile in suboxic conditions, allowing it to be readily incorporated into carbonate lattice (Barnaby and Rimstidt, 1989; Emerson and Hedges, 2008). Ce also turns mobile in low Eh environments and then becomes fixed when in contact with oxidizers (Bellanca et al., 1997; Haley et al., 2004). The shallow water setting of the dolomite interval is also indicated by the occurrences of exposure surfaces, likely resulted in oscillating penetration of oxygen into part of the sediment column (mud or microbialites), allowing for mobilization and sequestration of Ce in oxides. V/Cr and Ni/Co ratios also indicate suboxic environments (Jones and Manning, 1994). Although much of the Hevyon Formation would be interpreted to have been accumulated under dysoxic to suboxic conditions based on V/Cr and Ni/Co ratios, it is possible that these ratios have been modulated by redox pumping in the same fashion as Mn and Ce.

Similarly, depletion of ^{13}C in both dolostones and limestones from the Hevyon Formation relative to coeval marine limestones implies mineralization of isotopically light organic carbon (Katz et al., 2005), and this is further supported by the occurrence of residual organic matter (Fig. 1Si and j) in dolostones. One possible pathway for these reduced low energy (possibly stagnate) water, where organic matter can be degraded in the shallow sediment,

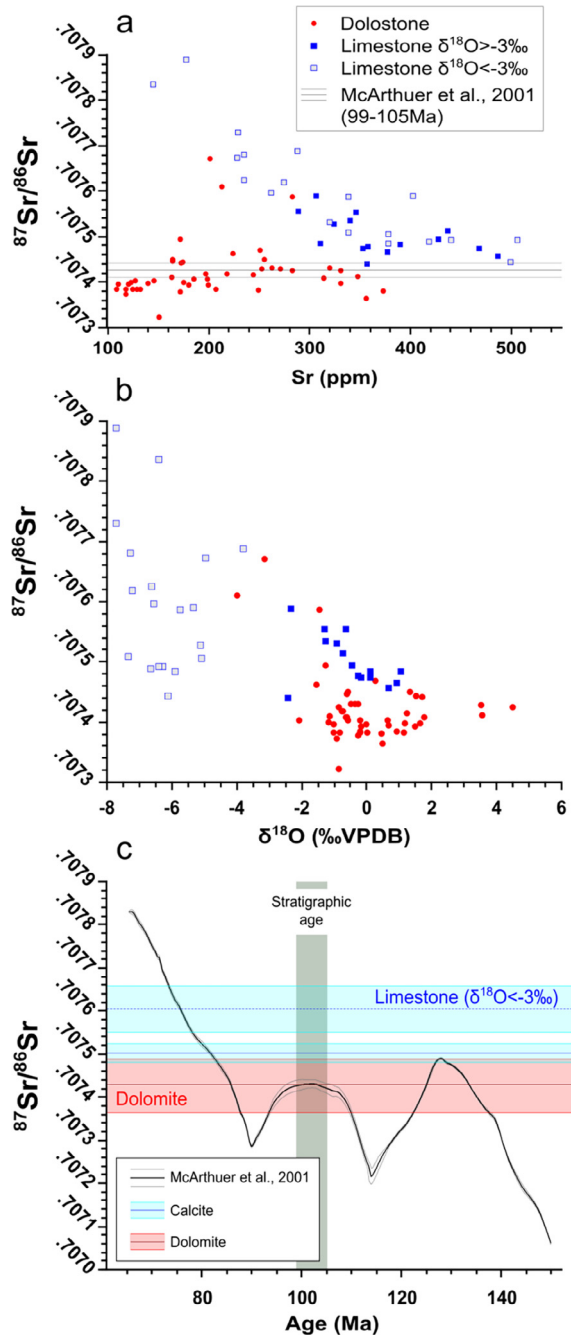


Fig. 10. (a) Plot of $^{87}\text{Sr}/^{86}\text{Sr}$ ratio versus Sr concentration for the carbonate samples. (b) Plot of $^{87}\text{Sr}/^{86}\text{Sr}$ ratios versus $\delta^{18}\text{O}$, (c) Comparison of the ranges of $^{87}\text{Sr}/^{86}\text{Sr}$ ratios for different carbonates with the seawater curve in geological history (McArthur et al., 2001). See text for discussion.

would be in a restricted basin, possibly a shallow epi-platform lagoon. Basin restriction would lead to increases in salinity and possible stagnation, which in turn promote dolomitization (Warren, 2000). This is confirmed with the occurrence of residual halite embedded in dolomite samples from Makhtesh Hatira (Fig. 1Sk and i; also Sandler and

Harlavan, 2006), as well as reports of embedded halite in rocks from a contemporary section further north (Sass and Katz, 1982).

Synthesizing the evidence above, the principal mechanism of dolomitization in the Hevyon Formation is interpreted to be microbial (Vasconcelos et al., 1995, 2006), occurring soon after initial deposition - within the soft sediment. Modern examples of microbial dolomitization include the shallow sabkha of Trucial coast (United Arab Emirates) where the microbially-mediated dolomite crystals precipitate from marine derived ground water (Bontognali et al., 2010; Geske et al., 2015a) as well as coastal lagoons such as Lagoa Vermelha or Brejo do Espinho Lagoon (Brazil) where dolomitization occurs within subaqueous microbial mats (Vasconcelos and McKenzie, 1997; Sánchez-Román et al., 2009). The microbial origin of dolostones from the Hevyon Formation is also supported by the consistency of $^{87}\text{Sr}/^{86}\text{Sr}$ ratios chemostratigraphy with stratigraphic age as well as sedimentary features and the small crystal size of the dolomite. The most notably fine laminated dolomitic microbialites are found primarily in the upper part of the unit (Fig. 3d), and microbialites are known to host dolomitization processes and produce fine-grained dolomite (Sánchez-Román et al., 2009; Krause et al., 2012).

The presence of shallow to intertidal facies in the case of the Hevyon Formation further suggests wave and tidal pumping, which advect water from the nearshore and within the pore space up to several kilometers from shore (Santos et al., 2012). These advection-dominated conditions would facilitate the supply of electron acceptors (i.e., O_2 , NO_3^- , Mn^{4+} , Fe^{3+} , and SO_4^{2-}) for microbial activities within the pore water. Indeed, Mn and Ce enrichment required an infusion of oxygen and dissolved species into the pore space, therefore the supply of electron acceptors such as NO_3^- , Mn^{4+} , Fe^{3+} and SO_4^{2-} were not limited within the shallow pore space.

Microbes in soft sediments can use a diverse metabolic pathway for their activities, and the metabolic mechanisms are dependent on the electron acceptors in the presence of abundant organic matters (Petash et al., 2017). In organic-rich sediment, the supply of electron acceptors by advection would fuel microbial activities that can catalyze dolomitization (Slaughter and Hill, 1991; Mazzullo, 2000; Petash et al., 2015; Petash et al., 2017). Given abundant supply of high energy-yielding species such as NO_3^- and Mn^{4+} in advection-dominated settings, microbial communities would preferentially utilize the metabolic pathways of nitrite reduction or Mn(IV)-reduction over the low energy-yielding sulphate reduction or methanogen pathways (Froelich et al., 1979; Emerson et al., 1979), which are more often utilized in diffusive dominated where the high energy-yielding species are more rapidly depleted (Petash et al., 2017). Advection would also have introduced seawater dissolved inorganic carbon (DIC) to the soft sediment to dilute the organic C isotope signature, which explains the only mildly negative $\delta^{13}\text{C}$ values of the dolomite from the Hevyon Formation.

5.4. Isotopic response of Mg to basin restriction

The shallow microbial origin of dolomite in advection-dominated sediments bears on its Mg isotope signatures. Prior studies of young carbonate platforms revealed an adequate exchange of Mg between dolomite and contemporaneous seawater in advection-dominated settings (Fantle and Higgins, 2014; Higgins et al., 2018). Therefore, dolomite of the Hevyon Formation should have been buffered by contemporaneous fluids overlying the sediment-seawater interface. The variability in $\delta^{26}\text{Mg}_{\text{dolo}}$ values, therefore, likely reflects changes in seawater during dolomite precipitation. Indeed, multiple cycles of oscillation in $\delta^{26}\text{Mg}$ occur across the dolomite section, and the most evident one is the increasing trend upsection between 60 m and 75 m (Fig. 6). Such increasing trend cannot be explained by downward diffusion of seawater/brine that dolomitized the calcium carbonate precursor in soft sediment, because an opposite trend of $\delta^{26}\text{Mg}$ versus depth would be expected in such process (e.g. Higgins and Schrag, 2010; Mavromatis et al., 2014; Huang et al., 2015). The best explanation is that Mg isotope composition of water mass within the basin was evolving at during dolomitization.

Geological evidence indicates events of shallowing and basin restriction during dolomite precipitation for the Hevyon Formation (Fig. 2). It should be noted that the residence time of Mg is on the order of ca. 10 Ma (Foster et al., 2010), therefore the Mg isotope composition of seawater in open oceans should not change over the time represented by the Hevyon Formation (Late Albian). However, within a restricted basin, precipitation of dolomite from seawater would preferentially remove light Mg isotopes from aqueous solution (Li et al., 2015), leaving heavier Mg isotopes in the water mass and leading to increases in $\delta^{26}\text{Mg}$ for the subsequent dolomite precipitates. The up-section increase in $\delta^{26}\text{Mg}$ of dolomite between 60 m and 75 m along the section (Fig. 6) is interpreted to reflect progressive dolomite precipitation in response to basin restriction. The dip in $\delta^{26}\text{Mg}$ at 75 m is indicative of a shift towards increased water exchange that replenished seawater Mg into the basin. Rhythmic variations in $\delta^{26}\text{Mg}$ of dolomite along the sedimentary column, therefore, are indicative of cycles of basin restriction and seawater replenishment during the deposition of the Hevyon Formation.

In addition to Mg isotope responses, dolomite precipitation in episodically restricted basin may also be associated with other mineralogical effects. In the Hevyon Formation, a transition from the Ca-dolomite in the lower half of the unit (<60 m) to the Mg-dolomite in the upper part of the unit (60–105 m, Fig. 2) implies an increase in Mg/Ca ratios in the fluids where dolomite was precipitated from Kaczmarek and Sibley (2011). The Mg/Ca ratio of Early Cretaceous seawater was much lower than the modern value, possibly close to 1 (Ries, 2004; Steuber and Rauch, 2005). Be the Mg/Ca ratio of the solution slightly higher than 1 (Dickson, 2004; Timofeeff et al., 2006), Ca in solution would be consumed more rapidly than Mg by dolomitization, and the residual solution Mg/Ca would increase, leading to the formation of Mg-rich dolomite. Moreover,

this indicates at least some level of restriction of the dolomitizing system. Otherwise, the replenishing flux will mute the effect of Mg and Ca drawdown by dolomite formation. By contrast, the decrease in $\text{MgCO}_3\%$ in dolomite at 75 m (Fig. 2) implies an abrupt decrease in Mg/Ca ratio of the aqueous solution, which should be caused by a major event of seawater replenishment, consistent with the Mg isotope record. Additionally, as the water body becomes more restricted, total ion concentrations increase with progressive evaporation. According to kinetic nucleation theory, increases in ionic concentrations and super-saturation index should result in higher nucleation rate (Katz and Donohue, 1979), leading to smaller crystal size in precipitates. Therefore, crystal size, stoichiometry, and Mg isotope compositions of dolomite are expected to correlate in a restricted basin setting, and the dolomite samples from the Hevyon Formation show the correlations as expected, that magnesium (% $\text{MgCO}_3 > 50\%$) dolomite have smaller crystal size (Fig. 4) and higher $\delta^{26}\text{Mg}$ values than calcium (% $\text{MgCO}_3 < 50\%$) dolomite (Fig. 9).

Assuming that removal of Mg from seawater with an initial value of $\delta^{26}\text{Mg}_{\text{SW0}}$ in an essentially closed system follows a Rayleigh process with a constant fractionation factor of $\epsilon_{\text{dolomite}}$, the Mg isotope compositions of the instantaneous dolomite precipitate ($\delta^{26}\text{Mg}_{\text{dolo-inst}}$) and the integrated (bulk) dolomite ($\delta^{26}\text{Mg}_{\text{dolo-bulk}}$) can be both described as functions of the fractional removal of magnesium (f_{Mg}):

$$\delta^{26}\text{Mg}_{\text{Dolo-inst}} = \delta^{26}\text{Mg}_{\text{SW0}} - \epsilon_{\text{dolomite}}(\ln(1 - f_{\text{Mg}}) - 1) \quad (1)$$

$$\delta^{26}\text{Mg}_{\text{Dolo-bulk}} = \delta^{26}\text{Mg}_{\text{SW0}} - \frac{1 - f_{\text{Mg}}}{f_{\text{Mg}}} \epsilon_{\text{dolomite}} \ln(1 - f_{\text{Mg}}) \quad (2)$$

Based on a static Mg isotope mass balance model, Li et al. (2015) calculated seawater $\delta^{26}\text{Mg}$ throughout the Phanerozoic and estimated that the Albian seawater had a $\delta^{26}\text{Mg}_{\text{SW0}}$ value of $-0.4\text{\textperthousand}$, which is higher than modern seawater values ($-0.8\text{\textperthousand}$; Ling et al., 2011). Using $\delta^{26}\text{Mg}_{\text{SW0}}$ of $-0.4\text{\textperthousand}$ and a constant Mg isotope fractionation factor ($\epsilon_{\text{dolomite}}$) of $-1.9\text{\textperthousand}$ (Li et al., 2015) during dolomite precipitation, the Mg isotope compositions of bulk and instantaneous dolomite precipitates, as well as modified seawater in a restricted basin, are calculated and plotted against the degree of Mg removal from the seawater (f_{Mg} ; Fig. 11).

For both seawater and instantaneous dolomite precipitate, $\delta^{26}\text{Mg}$ increase with continued Mg removal following a Rayleigh function. The increase in $\delta^{26}\text{Mg}$ of bulk dolomite is less dramatic due to the integrative effect as the $\delta^{26}\text{Mg}$ of bulk dolomite cannot exceed $\delta^{26}\text{Mg}_{\text{SW0}}$. When f_{Mg} is small (i.e., at the initial stage of basin restriction), both $\delta^{26}\text{Mg}_{\text{dolo-bulk}}$ and $\delta^{26}\text{Mg}_{\text{dolo-inst}}$ are the lowest and close to being in equilibrium with $\delta^{26}\text{Mg}_{\text{SW0}}$, which is $-2.3\text{\textperthousand}$. It is important to note that the lowest $\delta^{26}\text{Mg}$ value from the Hevyon Formation is also $-2.30 \pm 0.09\text{\textperthousand}$ (Fig. 9b), consistent with the model. $\delta^{26}\text{Mg}$ of dolomite from the Hevyon Formation varies by $0.8\text{\textperthousand}$, from $-2.30 \pm 0.09\text{\textperthousand}$ to $-1.52 \pm 0.02\text{\textperthousand}$ (Fig. 6). Such isotopic variability corresponds to a degree of removal of 34% and 63%

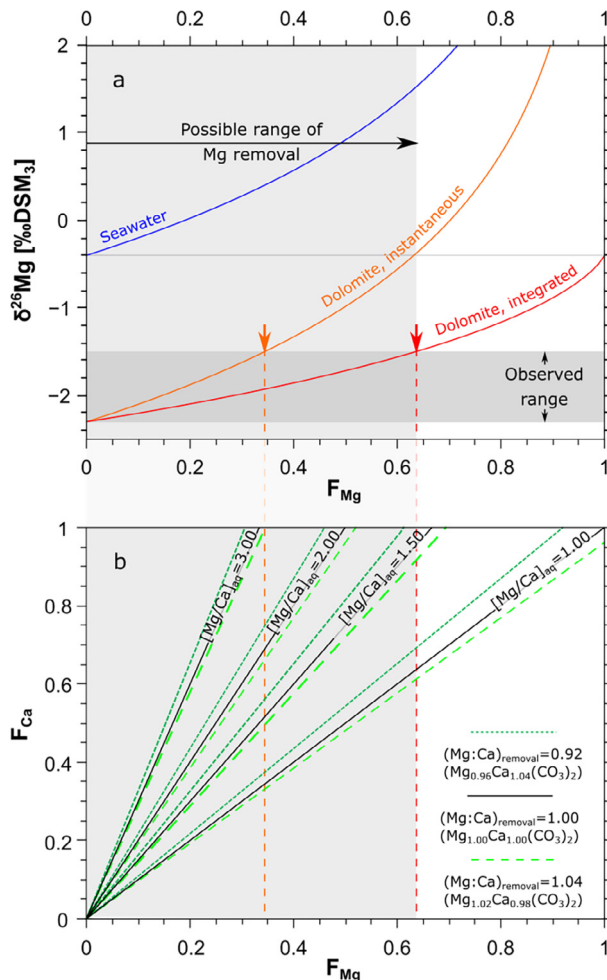


Fig. 11. Isotopic and elemental effects of Ca and Mg removal by dolomitization in a closed system. a. Evolution of $\delta^{26}\text{Mg}$ for seawater, instantaneous dolomite precipitate, and bulk dolomite precipitate with progressive removal of Mg from a closed system following a Rayleigh fractionation with $\epsilon = 1.9\text{‰}$ and $\delta^{26}\text{Mg}_{\text{sw0}} = -0.4\text{‰}$. (b) Relation between the degrees of Mg removal and Ca removal by dolomite precipitation from aqueous solutions of different initial Mg/Ca ratios.

according to the Rayleigh model for instantaneous dolomite precipitate and integrated bulk dolomite, respectively (Fig. 11).

Dolomite precipitation removes about equal amounts of Mg and Ca from the aqueous solution. Therefore the maximum degree of Mg removal from seawater by dolomite deposition is controlled by the initial Mg/Ca ratio of seawater. If the Mg/Ca ratio of seawater is close to 1:1, then a fairly large degree of Mg removal from aqueous solution is theoretically allowed. If Mg/Ca ratio is above 1, Ca would be depleted more rapidly than Mg from seawater by dolomitization and the maximum degree of Mg removal must be lower, limited by complete Ca depletion (Fig. 11b). Correspondingly, the variability in $\delta^{26}\text{Mg}$ of dolomite is lower due to the lower maximum f_{Mg} for seawater of high initial Mg/Ca ratio. A f_{Mg} of 34% (instantaneous dolomite) and 63% (bulk dolomite), as constrained from the measured

Mg isotope variability and the models (Fig. 11a) correspond to Mg/Ca ratio of about 3:1 and 1.5:1, respectively. It should be noted that the Mg isotope variability of 0.8‰ of the dolomite in the Hevyon Formation is measured only from a limited sample pool. Thus the actual Mg isotope variability could be greater. Therefore, the maximum f_{Mg} for seawater could be even higher. Moreover, it is unlikely to form dolomite from a solution of very little Ca (i.e., modified seawater with close to 100% removal of Ca). Therefore, the ratios of 3:1 and 1.5:1 are the upper limit of Albian seawater Mg/Ca ratios, the actual Mg/Ca ratio of Albian seawater should be more close to 1:1 than these theoretical upper limit. Such estimates are relatively insensitive to variations in the stoichiometry of dolomite precipitates (see dashed lines in Fig. 11b).

If we accept dolomite as the integrative precipitate from seawater, then Albian seawater should have an Mg/Ca ratio between 1.5 and 1. This range is consistent with previous studies that reconstructed coeval seawater Mg/Ca values from rudists (Steuber and Rauch, 2005), marine CaCO_3 veins (Coggon et al., 2010), halite fluid inclusion (Timofeeff et al., 2006) and geochemical models (Hardie, 1996; Farkaš et al., 2007, Fig. 12). A recent study also provided evidence for high Ca concentrations, and low SO_4^{2-} in Cretaceous seawater based on the Ca isotope record of evaporites (Blättler and Higgins, 2014), which supports a low Mg/Ca ratio, with low SO_4^{2-} possibly plays into

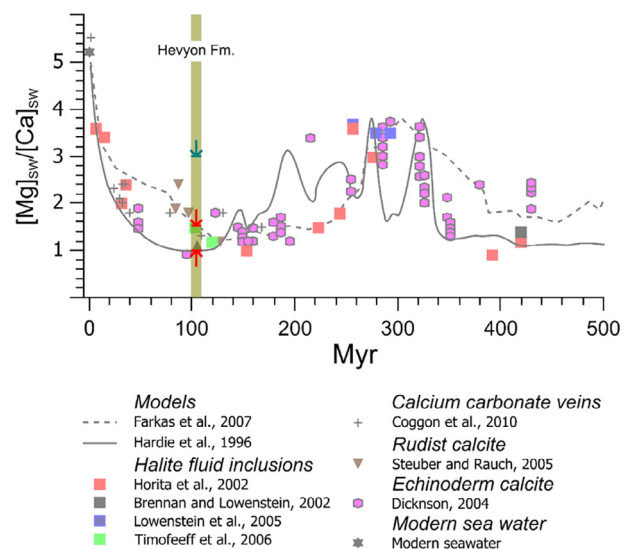


Fig. 12. Reconstruction of the Mg/Ca ratio of seawater over the Phanerozoic from models (Hardie, 1996; Farkaš et al., 2007), halite fluid inclusions (Brennan and Lowenstein, 2002; Horita et al., 2002; Lowenstein et al., 2005; Timofeeff et al., 2006), marine calcium carbonate veins (Coggon et al., 2010), and biogenic calcite from Rudists (Steuber and Rauch, 2005) and Echinoderms (Dickson, 2004), as well as from this Mg isotope study. The vertical bar indicates the age range of the Hevyon Formation, and the arrows indicate possible Mg/Ca range based on $\delta^{26}\text{Mg}$ variability and Rayleigh models (Red arrows for the integrated precipitate, glaucous for instantaneous precipitate, see Fig. 11). (For interpretation of the references to color in this figure legend, the reader is referred to the web version of this article.)

promoting early dolomitization (Morrow and Ricketts, 1988). Magnesium isotopes in dolomite, therefore, provide a novel and independent approach to constrain seawater Mg/Ca ratio.

5.5. Geological Implications

Formation of dolomite is known to occur in multiple geological settings, including lacustrine, mixing zones, palustrine, sabkhas, lagoons, reefs and hydrothermal settings (Warren, 2000). The behavior of Mg isotopes during dolomitization would differ between these settings (Geske et al., 2015b), that some of Mg isotope variability may stem from diagenetic windows (Blättler et al., 2015) or relate to hydrothermal conditions (Geske et al., 2012; Walter et al., 2015). As such, it is important to characterize each of these settings within its sedimentological, diagenetic, and post-depositional context for Mg isotope studies. The Hevyon Formation is a typical section of hinterland attached carbonate platform with an exceptionally well preserved dolostone unit. The Hevyon Formation exhibits large-scale shallowing and deepening cycles that coincide with facies and mineralogical changes, and therefore is an ideal natural laboratory for understanding Mg isotope behavior in hinterland attached carbonate platforms, an important dolomitization setting.

The case of Hevyon Formation suggests that detailed analyses of stratigraphic isotopic variation of Mg in dolomite sequence allow identification of cycles of restriction and seawater replenishment in carbonate platforms. Specifically, the increase in dolomite abundance coincides with the increase in $\delta^{26}\text{Mg}$ and the occurrence of exposure events, and the inversion of the trend with deepening (Fig. 7). Although basin restriction and increased removal of Mg by dolomitization would cause a significant variation in $\delta^{26}\text{Mg}_{\text{dolo}}$, constraints on $\delta^{26}\text{Mg}$ of seawater can still be made, as long as one can identify the dolomite that was formed in the earliest stage of a seawater replenishment cycle or from non-modified seawater buffered setting. Allowing for these, and with other Mg sources ruled out, the lowest $\delta^{26}\text{Mg}$ values may be used to infer the Mg isotope composition of the least-evolved aqueous solution or seawater.

Dolomite precipitation under an ideal condition of restriction would follow a Rayleigh function for both elemental and isotopic signals. In this case, Mg/Ca ratio of the seawater would act as a key factor that constrains the upper limit of the proportion of Mg in a solution that can be removed from the aqueous solution, due to the stoichiometry of dolomite. The degree of Mg removal from aqueous solution, in turn, controls the Mg isotope variability in precipitated dolomite. Therefore, in cases of restricted basin, not only the relative trends of increasing or decreasing $\delta^{26}\text{Mg}$ in a dolomite sequence can be used to identify events of restriction or connection, but also the absolute maximum variability in $\delta^{26}\text{Mg}$ in dolomite sequence can be used to infer Mg/Ca ratios of contemporary seawater. We note that such scenario is simplified and requires a combination of conditions that are usually difficult to be strictly satisfied in real geological settings, which may be

complicated by other inputs such as riverine runoffs, as well as deposition of multiple carbonates (e.g., calcite) in addition to dolomite. Nevertheless, this evidence provides an alternative way to constrain the decoupling of epicontinental seas from the open ocean (Holmden et al., 1998).

The case of Hevyon Formation does suggest dolomite precipitation can be the dominant carbonate precipitation pathway for a water mass, and the fact that the seawater Mg/Ca ratio inferred from Mg isotope variability data matches other estimates so well (Fig. 12) implies the validity of the Rayleigh model in principle. Last but not least, this study provides an alternative theoretical framework to interpret the Mg isotope variability in dolomite records other than the diffusion-reaction model that emphasizes diagenetic processes (Higgins and Schrag, 2010; Fantle and Higgins, 2014; Mavromatis et al., 2014; Huang et al., 2015; Higgins et al., 2018).

6. CONCLUSIONS

In this study, we performed a detailed investigation of the upper Albian Hevyon Formation in southern Israel that integrated field description, petrography, mineralogy, elemental and isotopic geochemistry. Based on geological evidence and $^{87}\text{Sr}/^{86}\text{Sr}$ data, dolomitization of the Hevyon Formation occurred contemporaneously to sedimentation and coincided with shallowing of the water level in the basin. The high Mn content and positive Ce anomaly, as well as elevated Ni/Co and V/Cr ratios in conjunction with low $\delta^{13}\text{C}$ in the carbonates, indicate prevalent suboxic conditions during process of dolomitization. Combining the above geochemical evidence and the prevalence of microbialites, formation of dolomite is interpreted to be microbially-mediated and buffered by contemporaneous seawater in an episodically restricted and replenished basin during the Early Cretaceous.

Oxygen isotope data suggest that the majority of carbonate samples from Hevyon Formation are well preserved and free of burial resetting, particularly for dolomite phases. $\delta^{26}\text{Mg}$ values of dolomite from the Hevyon Formation vary from $-2.30\text{\textperthousand}$ to $-1.52\text{\textperthousand}$, and show a weak negative correlation with crystal size, and a positive correlation with Mg/Ca ratio of dolomite. These are interpreted to be the results of dolomite precipitation from evolved seawater in a restricted basin. Fluctuations in $\delta^{26}\text{Mg}$ across the stratigraphic column of the dolomite strata, therefore mark events of basin restriction and seawater replenishment. Furthermore, it is possible to infer initial $\delta^{26}\text{Mg}$ and Mg/Ca of coeval seawater from a large dolomite $\delta^{26}\text{Mg}$ dataset based on a Rayleigh distillation model for the water mass in an isolated basin, and an Mg/Ca of 1–1.5 has been estimated for Albian seawater.

This study of the Hevyon Formation showcases the complexity of Mg isotope behavior in carbonate platform settings and thus highlights the necessity of performing integrated and detailed analyses that combines sedimentology and isotope geochemistry in order to understand natural Mg isotope variability in carbonate records. Possible intra-basinal effects, therefore, need to be taken into consideration in attempts to apply Mg isotopes in early diagenetic

dolomite to study seawater chemistry, and a high-density and systematic sampling strategy is preferred over random and low-density sampling.

ACKNOWLEDGEMENT

This study was jointly supported by ISF grant No. 2208/15 to NDW and NSFC grant No. 41561144002 to WL, based on research agreements between the Israeli Science Foundation and the National Science Foundation of China. WL also acknowledges supports from NSFC with grants Nos. 41473002 and 41622301. Special thanks are given to Gerald Auer for his input regarding the redox proxies. Nimer Taha provided assistance for analytical work at the Basin Analysis and Petrophysical laboratory (Petro-Lab), University of Haifa. NDW also thanks the Wolfson Family Charitable Trust for supporting the purchase of some of the analytical equipment used in the context of this study. The authors thank Adrian Immenhauser, Matthew Fantle, an anonymous reviewer and editor Fangzhen Teng for constructive comments.

APPENDIX A. SUPPLEMENTARY MATERIAL

Supplementary data associated with this article can be found, in the online version, at <https://doi.org/10.1016/j.gca.2018.05.024>. These data include Google maps of the most important areas described in this article.

REFERENCES

- Ahr W. (2008) *Geology of Carbonate Reservoirs*. John Wiley & Sons, Hoboken.
- Alsharhan A. S. and Kendall C. G. S. C. (1991) Cretaceous chronostratigraphy, unconformities and eustatic sealevel changes in the sediments of Abu Dhabi, United Arab Emirates. *Cretac. Res.* **12**, 379–401.
- Arvidson R. S., Guidry M. W. and Mackenzie F. T. (2011) Dolomite controls on phanerozoic seawater chemistry. *Aquat. Geochem.* **17**, 735–747.
- Bailey T. R., McArthur J. M., Prince H. and Thirlwall M. F. (2000) Dissolution methods for strontium isotope stratigraphy: whole rock analysis. *Chem. Geol.* **167**, 313–319.
- Barnaby R. J. and Rimstidt J. D. (1989) Redox conditions of calcite cementation interpreted from Mn and Fe contents of authigenic calcites. *Geol. Soc. Am. Bull.* **101**, 795–804.
- Bein A. and Weiler Y. (1976) The Cretaceous Talme Yafe Formation: a contour current shaped sedimentary prism of calcareous detritus at the continental margin of the Arabian Craton. *Sedimentology* **23**, 511–532.
- Bellanca A., Masetti D. and Neri R. (1997) Rare earth elements in limestone/marlstone couplets from the Albian-Cenomanian Cismon section (Venetian region, northern Italy): assessing REE sensitivity to environmental changes. *Chem. Geol.* **141**, 141–152.
- Bialik O. M. and Waldmann N. (2017) The drowning of a siliciclastic shelf: Insights into oceanographic reconstructions of the northern Arabian Platform during the Early Cretaceous. *Basin Res.*
- Blättler C. L. and Higgins J. A. (2014) Calcium isotopes in evaporites record variations in Phanerozoic seawater SO₄ and Ca. *Geology* **42**, 711–714.
- Blättler C. L., Miller N. R. and Higgins J. A. (2015) Mg and Ca isotope signatures of authigenic dolomite in siliceous deep-sea sediments. *Earth Planet. Sci. Lett.* **419**, 32–42.
- Bontognali T. R. R., Vasconcelos C., Warthmann R. J., Bernasconi S. M., Dupraz C., Strohmenger C. J. and McKenzie J. A. (2010) Dolomite formation within microbial mats in the coastal sabkha of Abu Dhabi (United Arab Emirates). *Sedimentology* **57**, 824–844.
- Braun M. and Hirsch F. (1994) Mid Cretaceous (Albian-Cenomanian) carbonate platforms in Israel. *Cuad. Geol. Ibérica* **18**, 59–81.
- Brennan S. and Lowenstein T. (2002) The major-ion composition of Silurian seawater. *Geochim. Cosmochim. Acta* **66**, 2683–2700.
- Chanda P. and Fantle M. S. (2017) Quantifying the effect of diagenetic recrystallization on the Mg isotopic composition of marine carbonates. *Geochim. Cosmochim. Acta* **204**, 219–239.
- Coggon R. M., Teagle D. a. H., Smith-Duque C. E., Alt J. C. and Cooper M. J. (2010) Reconstructing past seawater Mg/Ca and Sr/Ca from mid-ocean ridge flank calcium carbonate veins. *Science* **327**(80), 1114–1117.
- Davies T. A. and Worsley T. R. (1981) *Paleoenvironmental implications of oceanic carbonate sedimentation rates*. SEPM Special Publication, pp. 169–179.
- De Muynck D., Huelga-Suarez G., Van Hege L., Degryse P. and Vanhaecke F. (2009) Systematic evaluation of a strontium-specific extraction chromatographic resin for obtaining a purified Sr fraction with quantitative recovery from complex and Ca-rich matrices. *J. Anal. At. Spectrom.* **24**, 1498.
- Dickson J. A. D. (2004) Echinoderm skeletal preservation; calcite- aragonite seas and the Mg/Ca ratio of Phanerozoic oceans. *J. Sediment. Res.* **74**, 355–365.
- Emerson S. R. and Hedges J. I. (2008) *Chemical Oceanography and the Marine Carbon Cycle*. Cambridge University Press, Cambridge.
- Emerson S., Cranston R. E. and Liss P. S. (1979) Redox species in a reducing fjord: equilibrium and kinetic considerations. *Deep Sea Res. Part A. Oceanogr. Res. Pap.* **26**, 859–878.
- Eppelbaum L. (1996) Geothermal investigations in the Dead Sea Rift zone, Israel: implications for petroleum geology. *J. Pet. Geol.* **19**, 425–444.
- Erbacher J., Hemleben C., Huber B. T. and Markey M. (1999) Correlating environmental changes during early Albian oceanic anoxic event 1B using benthic foraminiferal paleoecology. *Mar. Micropaleontol.* **38**, 7–28.
- Fantle M. S. and Higgins J. (2014) The effects of diagenesis and dolomitization on Ca and Mg isotopes in marine platform carbonates: implications for the geochemical cycles of Ca and Mg. *Geochim. Cosmochim. Acta* **142**, 458–481.
- Farkaš J., Böhm F., Wallmann K., Blenkinsop J., Eisenhauer A., van Geldern R., Munnecke A., Voigt S. and Veizer J. (2007) Calcium isotope record of Phanerozoic oceans: implications for chemical evolution of seawater and its causative mechanisms. *Geochim. Cosmochim. Acta* **71**, 5117–5134.
- Fisher W. L. and Rodda P. U. (1969) Edwards formation (lower cretaceous), Texas: dolomitization in a carbonate platform system. *Am. Assoc. Pet. Geol. Bull.* **53**.
- Flood P. G. and Chivas A. R. (1995) Origin of massive dolomite, leg 143, hole 866a, resolution guyot, 1 mid-pacific mountains. *Proc. Ocean Drill. Progr. – Sci. Results* **143**, 161–169.
- Flügel E. (2010) *Microfacies of Carbonate Rocks*. Springer, Berlin, Heidelberg.
- Föllmi K. B. and Gainon F. (2008) Demise of the northern Tethyan Urgonian carbonate platform and subsequent transition towards pelagic conditions: the sedimentary record of the Col de la Plaine Morte area, central Switzerland. *Sediment. Geol.* **205**, 142–159.
- Foster G. L., Pogge von Strandmann P. A. E. and Rae J. W. B. (2010) Boron and magnesium isotopic composition of seawater. *Geochim., Geophys., Geosyst.* **11**, n/a–n/a.

- Froelich P. N., Klinkhammer G. P., Bender M. L., Luedtke N. A., Heath G. R., Cullen D., Dauphin P., Hammond D., Hartman B. and Maynard V. (1979) Early oxidation of organic matter in pelagic sediments of the eastern equatorial Atlantic: suboxic diagenesis. *Geochim. Cosmochim. Acta* **43**, 1075–1090.
- Galy A., Yoffe O., Janney P. E., Williams R. S., Cloquet C., Alard O., Halicz L., Wadhwa M., Hutcheon I. D., Ramon E. and Carignan J. (2003) Magnesium isotope heterogeneity of the isotopic standard SRM980 and new reference materials for magnesium-isotope-ratio measurements. *J. Anal. At. Spectrom.* **18**, 1352–1356.
- Gardosh M., Weimer P. and Flexer A. (2011) The sequence stratigraphy of Mesozoic successions in the Levant margin, southwestern Israel: a model for the evolution of southern Tethys margins. *Am. Assoc. Pet. Geol. Bull.* **95**, 1763–1793.
- Geske A., Zorlu J., Richter D., Buhl D., Niedermayr A. and Immenhauser A. (2012) Impact of diagenesis and low grade metamorphism on isotope ($\delta^{26}\text{Mg}$, $\delta^{13}\text{C}$, $\delta^{18}\text{O}$ and $\delta^{87}\text{Sr}/\delta^{86}\text{Sr}$) and elemental (Ca, Mg, Mn, Fe and Sr) signatures of Triassic sabkha dolomites. *Chem. Geol.* **332–333**, 45–64.
- Geske A., Lokier S., Dietzel M., Richter D. K., Buhl D. and Immenhauser A. (2015a) Magnesium isotope composition of sabkha porewater and related (sub-)recent stoichiometric dolomites, Abu Dhabi (UAE). *Chem. Geol.* **393–394**, 112–124.
- Geske A., Goldstein R. H., Mavromatis V., Richter D. K., Buhl D., Kluge T., John C. M. and Immenhauser A. (2015b) The magnesium isotope ($\delta^{26}\text{Mg}$) signature of dolomites. *Geochim. Cosmochim. Acta* **149**, 131–151.
- Given R. K. and Wilkinson B. H. (1987) Dolomite abundance and stratigraphic age: constraints on rates and mechanisms of phanerozoic dolostone formation. *J. Sediment. Petrol.* **57**, 1068–1078.
- Goldsmith J. R. and Graf D. L. (1958) Relation between lattice constants and composition of the Ca-Mg carbonates. *Am. Mineral.* **43**, 84–101.
- Graf D. and Goldsmith J. (1956) Some hydrothermal syntheses of dolomite and protodolomite. *J. Geol.* **64**, 173–186.
- Gvirtzman Z. (2004) Chronostratigraphic table and subsidence curves of Southern Israel. *Isr. J. Earth Sci.* **53**, 47–61.
- Haley B. A., Klinkhammer G. P. and McManus J. (2004) Rare earth elements in pore waters of marine sediments. *Geochim. Cosmochim. Acta* **68**, 1265–1279.
- Haq B. U. and Al-Qahtani A. M. (2005) Phanerozoic cycles of sea-level change on the Arabian Platform. *GeoArabia* **10**, 127–160.
- Hardie L. a. (1996) Secular variation in seawater chemistry: an explanation for the coupled secular variation in the mineralogies of marine limestones and potash evaporites over the past 600 m.y. *Geology* **24**, 279.
- Haworth M., Hesselbo S. P., McElwain J. C., Robinson S. A. and Brunt J. W. (2005) Mid-cretaceous pCO₂ based on stomata of the extinct conifer Pseudofrenelopsis (Cheirolepidiaceae). *Geology* **33**, 749.
- Hay W. W., Sloan J. L. and Wold C. N. (1988) Mass/age distribution and composition of sediments on the ocean floor and the global rate of sediment subduction. *J. Geophys. Res. Solid Earth* **93**, 14933–14940.
- Hay W. W., DeConto R., Wold C. N., Wilson K. M., Voigt S., Schulz M., Wold-Rossby A., Dullo W.-C., Ronov A. B., Balukhovsky A. N. and Söding E. (1999) Alternative global Cretaceous paleogeography. Geological Society of America Special Paper 332, Boulder, pp. 1–47.
- Higgins J. A. J. and Schrag D. P. (2010) Constraining magnesium cycling in marine sediments using magnesium isotopes. *Geochim. Cosmochim. Acta* **74**, 5039–5053.
- Higgins J. A., Blättler C. L., Lundstrom E. A., Santiago-Ramos D. P., Akhtar A. A., Crüger Ahm A.-S. A.-S., Bialik O., Holmden C., Bradbury H., Murray S. T. and Swart P. K. (2018) Mineralogy, early marine diagenesis, and the chemistry of shallow-water carbonate sediments. *Geochim. Cosmochim. Acta* **220**, 512–534.
- Hirsch F. and Braun M. (1994) Mid Cretaceous (Albian-Cenomanian) carbonate platforms in Israel. *Cuad. Geol. Iber.* **18**, 59–81.
- Holmden C., Creaser R. A., Muehlenbachs K., Leslie S. A. and Bergström S. M. (1998) Isotopic evidence for geochemical decoupling between ancient epeiric seas and bordering oceans: implications for secular curves. *Geology* **26**, 567–570.
- Horita J., Zimmermann H. and Holland H. (2002) Chemical evolution of seawater during the Phanerozoic Implications from the record of marine evaporites. *Geochim. Cosmochim. Acta* **66**, 3733–3756.
- Horita J. (2014) Oxygen and carbon isotope fractionation in the system dolomite–water–CO₂ to elevated temperatures. *Geochim. Cosmochim. Acta* **129**, 111–124.
- Hu Z., Hu W., Wang X., Lu Y., Wang L., Liao Z. and Li W. (2017) Resetting of Mg isotopes between calcite and dolomite during burial metamorphism: outlook of Mg isotopes as geothermometer and seawater proxy. *Geochim. Cosmochim. Acta* **208**, 24–40.
- Huang K.-J., Shen B., Lang X.-G., Tang W.-B., Peng Y., Ke S., Kaufman A. J., Ma H.-R. and Li F.-B. (2015) Magnesium isotopic compositions of the Mesoproterozoic dolostones: implications for Mg isotopic systematics of marine carbonates. *Geochim. Cosmochim. Acta* **164**, 333–351.
- Husson J. M., Higgins J. A., Maloof A. C. and Schoene B. (2015) Ca and Mg isotope constraints on the origin of Earth's deepest C excursion. *Geochim. Cosmochim. Acta* **160**, 243–266 <http://linkinghub.elsevier.com/retrieve/pii/S0016703715001544>.
- Ibrahim M. I. A. (2003) Late Albian – Middle Cenomanian palynofacies and palynostratigraphy, Abu Gharadig-5 well, Western Desert, Egypt, pp. 775–788.
- Jacobson A. D., Zhang Z., Lundstrom C. and Huang F. (2010) Behavior of Mg isotopes during dedolomitization in the Madison Aquifer, South Dakota. *Earth Planet. Sci. Lett.* **297**, 446–452 <http://linkinghub.elsevier.com/retrieve/pii/S0012821X10004139>.
- Jaglarz P. and Uchman A. (2010) A hypersaline ichnoassemblage from the Middle Triassic carbonate ramp of the Taticum domain in the Tatra Mountains, Southern Poland. *Palaeogeogr. Palaeoclimatol. Palaeoecol.* **292**, 71–81 <http://linkinghub.elsevier.com/retrieve/pii/S0031018210001550>.
- Jenkins D., Harms J. C. and Oesley T. W. (1984) Mesozoic sediments of Gebel Maghara, north Sinai, ARE. In *Proceedings of the 6th Exploration Seminar, Cairo*. Egyptian General Petroleum Corporation, pp. 130–158.
- Jones B. and Manning D. A. C. (1994) Comparison of geochemical indices used for the interpretation of palaeoredox conditions in ancient mudstones. *Chem. Geol.* **111**, 111–129.
- Kaczmarek S. E. and Sibley D. F. (2011) On the evolution of dolomite stoichiometry and cation order during high-temperature synthesis experiments: an alternative model for the geochemical evolution of natural dolomites. *Sediment. Geol.* **240**, 30–40.
- Katz J. L. and Donohue M. D. (1979) A kinetic approach to homogeneous nucleation theory. *Adv. Chem. Phys.* **40**, 137–155 <http://doi.wiley.com/10.1002/9780470142592>.
- Katz M. E., Wright J. D., Miller K. G., Cramer B. S., Fennell K. and Falkowski P. G. (2005) Biological overprint of the geological carbon cycle. *Mar. Geol.* **217**, 323–338.
- Kiessling W., Flügel E. and Golonka J. (1999) Paleoreef maps : evaluation of a comprehensive database on phanerozoic reefs. *Am. Assoc. Pet. Geol. Bull.* **10**, 1552–1587.

- Kiessling W., Flügel E. and Golonka J. (2003) Patterns of phanerozoic carbonate platform sedimentation. *Lethaia* **36**, 195–225.
- Koutsoukos E. A., Destro N., De Azambuja Filho NC. and Spadini A. R. (1993) *Upper Aptian-Lower Coniacian carbonate sequences in the Sergipe Basin, northeastern Brazil*. AAPG Memoir 56, Tulsa, pp. 127–144.
- Krause S., Liebetrau V., Gorb S., Sanchez-Roman M., McKenzie J. A. and Treude T. (2012) Microbial nucleation of Mg-rich dolomite in exopolymeric substances under anoxic modern seawater salinity: new insight into an old enigma. *Geology* **40**, 587–590.
- Lewy Z. (1988) Lithostratigraphic subdivision of the Hazera Formation (Late Albian-Late Cenomanian) in the Negev, southern Israel. *Isr. J. Earth Sci.* **37**, 205–210.
- Li W., Beard B. L. and Johnson C. M. (2011) Exchange and fractionation of Mg isotopes between epsomite and saturated MgSO₄ solution. *Geochim. Cosmochim. Acta* **75**, 1814–1828.
- Li W., Chakraborty S., Beard B. L. B., Romanek C. S. and Johnson C. M. (2012) Magnesium isotope fractionation during precipitation of inorganic calcite under laboratory conditions. *Earth Planet. Sci. Lett.* **333–334**, 304–316.
- Li W., Beard B., Li C. and Johnson C. (2014) Magnesium isotope fractionation between brucite and Mg aqueous species: implications for silicate weathering and biogeochemical. *Earth Planet. Sci. Lett.* **394**, 82–93.
- Li W., Beard B. L., Li C., Xu H. and Johnson C. M. (2015) Experimental calibration of Mg isotope fractionation between dolomite and aqueous solution and its geological implications. *Geochim. Cosmochim. Acta* **157**, 164–181.
- Li F.-B., Teng F. Z., Chen J. T., Huang K. J., Wang S. J., Lang X. G., Ma H. R., Peng Y. B. and Shen B. (2016) Constraining ribbon rock dolomitization by Mg isotopes: Implications for the “dolomite problem”. *Chem. Geol.* **445**, 208–220.
- Ling M.-X., Sedaghatpour F., Teng F.-Z., Hays P. D., Strauss J. and Sun W. (2011) Homogeneous magnesium isotopic composition of seawater: an excellent geostandard for Mg isotope analysis. *Rapid Commun. Mass Spectrom.* **25**, 2828–2836.
- Lowenstein T. K., Timofeeff M. N., Kovalevych V. M. and Horita J. (2005) The major-ion composition of Permian seawater. *Geochim. Cosmochim. Acta* **69**, 1701–1719.
- MacEachern J. A., Pemberton S. G., Gingras M. K. and Bann K. L. (2010) *Ichnology and facies models*. Geological Association of Canada, St. John's, NL, pp. 19–57.
- Machel H. G. (2004) Concepts and models of dolomitization: a critical reappraisal. *Geol. Soc. London Spec. Publ.* **235**, 7–63.
- Masse J., Borgoman J. and Al Maskiry S. (1997) Stratigraphy and tectonosedimentary evolution of a late Aptian-Albian carbonate margin: the northeastern Jebel Akhdar (Sultanate of Oman). *Sediment. Geol.* **113**, 269–280.
- Mavromatis V., Meister P. and Oelkers E. H. (2014) Using stable Mg isotopes to distinguish dolomite formation mechanisms: a case study from the Peru Margin. *Chem. Geol.* **385**, 84–91.
- Mavromatis V., Purgstaller B., Dietzel M., Buhl D., Immenhauser A. and Schott J. (2017) Impact of amorphous precursor phases on magnesium isotope signatures of Mg-calcite. *Earth Planet. Sci. Lett.* **464**, 227–236.
- Mazzullo S. J. (2000) Organogenic dolomitization in peritidal to deep-sea sediments. *SEPM J. Sediment. Res.* **70**, 10–23.
- McArthur A. J. M., Howarth R. J., Bailey T. R., McArthur J. M., Howarth R. J. and Bailey T. R. (2001) Strontium isotope stratigraphy: LOWESS version 3: best fit to the marine Sr-isotope curve for 0–509 Ma and accompanying look-up table for deriving numerical age. *J. Geol.* **109**, 155–170.
- Meister P. (2013) Two opposing effects of sulfate reduction on carbonate precipitation in normal marine, hypersaline, and alkaline environments. *Geology* **41**, 499–502.
- Morrow D. and Ricketts B. (1988) *Experimental investigation of sulfate inhibition of dolomite and its mineral analogues*. SEPM Special publications 43, Tulsa, pp. 25–38.
- Peng Y., Shen B., Lang X.-G., Huang K.-J., Chen J.-T., Yan Z., Tang W., Ke S., Ma H.-R. and Li F.-B. (2016) Constraining dolomitization by Mg isotopes: a case study from partially dolomitized limestones of the middle Cambrian Xuzhuang Formation, North China. *Geochem. Geophys. Geosyst.* **17**, 1109–1129.
- Petrasch D. A., Lalonde S. V., González-Arismendi G., Gordon R. A., Méndez J. A., Gingras M. K. and Konhauser K. O. (2015) Can Mn-S redox cycling drive sedimentary dolomite formation? A hypothesis. *Chem. Geol.* **404**, 27–40.
- Petrasch D. A., Bialik O. M., Bontognali T. R., Vasconcelos C., Roberts J. A., McKenzie J. A. and Konhauser K. O. (2017) Microbially catalyzed dolomite formation: from near-surface to burial. *Earth-Sci. Rev.* **171**, 558–582.
- Riechelmann S., Mavromatis V., Buhl D., Dietzel M., Eisenhauer A. and Immenhauser A. (2016) Impact of diagenetic alteration on brachiopod shell magnesium isotope ($\delta^{26}\text{Mg}$) signatures: experimental versus field data. *Chem. Geol.* **440**, 191–206.
- Ries J. B. (2004) Effect of ambient Mg/Ca ratio on Mg fractionation in calcareous marine invertebrates: A record of the oceanic Mg/Ca ratio over the Phanerozoic. *Geology* **32**, 981.
- Rodríguez-Aranda J. and Calvo J. (1998) Trace fossils and rhizoliths as a tool for sedimentological and palaeoenvironmental analysis of ancient continental evaporite successions. *Palaeogeogr. Palaeoclimatol. Palaeoecol.* **140**, 383–399.
- Rollion-Bard C., Saulnier S., Vigier N., Schumacher A., Chaussidon M. and Lécuyer C. (2016) Variability in magnesium, carbon and oxygen isotope compositions of brachiopod shells: Implications for paleoceanographic studies. *Chem. Geol.* **423**, 49–60.
- Sánchez-Román M., Vasconcelos C., Warthmann R. J., Rivadeneyra M. and McKenzie J. A. (2009) *Microbial dolomite precipitation under aerobic conditions: results from Brejo do Espinho Lagoon (Brazil) and culture experiments*. IAS Special Publications 41, Wiley-Blackwell, pp. 1–35.
- Sandler A. and Harlavan Y. (2006) Early diagenetic illitization of illite-smectite in Cretaceous sediments (Israel): evidence from K-Ar dating. *Clay Miner.* **41**, 637–658.
- Santos I. R., Eyre B. D. and Huettel M. (2012) The driving forces of porewater and groundwater flow in permeable coastal sediments: a review. *Estuar. Coast. Shelf Sci.* **98**, 1–15.
- Sass E. and Katz A. (1982) The origin of platform dolomites; new evidence. *Am. J. Sci.* **282**, 1184–1213.
- Scott R. W. (1990) Chronostratigraphy of the Cretaceous carbonate shelf, southeastern Arabia. In *The Geology and Tectonics of the Oman Region*. Geological Society Special Publication 49, London, pp. 89–108.
- Segev A. and Sass E. (2009) *Geology of Mt. Carmel, Jerusalem*. Sharland P. R., Archer R., Casey D. M., Davies R. B., Hall S. H., Heward A. P., Horbury A. D. and Simmons M. D. (2001) *Arabian Plate Sequence Stratigraphy*. Gulf PetroLink, Bahrain.
- Sharp Z. (2007) *Principles of Stable Isotope Geochemistry*. Pearson Education, London.
- Slaughter M. and Hill R. J. (1991) The influence of organic matter in organogenic dolomitization. *J. Sediment. Petrol.* **61**, 296–303.
- Steuber T. and Bachmann M. (2002) Upper Aptian-Albian rudist bivalves from northern Sinai, Egypt. *Palaeontology* **45**, 725–749.

- Steuber T. and Rauch M. (2005) Evolution of the Mg/Ca ratio of Cretaceous seawater: implications from the composition of biological low-Mg calcite. *Mar. Geol.* **217**, 199–213.
- Teng F. Z., Li W. Y., Ke S., Yang W., Liu S. A., Sedaghatpour F., Wang S. J., Huang K. J., Hu Y., Ling M. X., Xiao Y., Liu X. M., Li X. W., Gu H. O., Sio C. K., Wallace D. A., Su B. X., Zhao L., Chamberlin J., Harrington M. and Brewer A. (2015) Magnesium isotopic compositions of international geological reference materials. *Geostand. Geoanalytical Res.* **39**, 329–339.
- Teng F.-Z. (2017) Magnesium isotope geochemistry. In *Reviews in Mineralogy and Geochemistry*, pp. 219–287.
- Teng F.-Z. and Yang W. (2014) Comparison of factors affecting the accuracy of high-precision magnesium isotope analysis by multi-collector inductively coupled plasma mass spectrometry. *Rapid Commun. Mass Spectrom.* **28**, 19–24.
- Timofeeff M. N., Lowenstein T. K., da Silva M. A. M. and Harris N. B. (2006) Secular variation in the major-ion chemistry of seawater: evidence from fluid inclusions in Cretaceous halites. *Geochim. Cosmochim. Acta* **70**, 1977–1994.
- Tipper E. T., Galy A. and Gaillardet J. (2006) The magnesium isotope budget of the modern ocean: constraints from riverine magnesium isotope ratios. *Earth Planet. Sci. Lett.* **250**, 241–253.
- Vahrenkamp V. and Swart P. (1994) Late Cenozoic dolomites of the Bahamas: metastable analogues for the genesis of ancient platform dolomites. In *Dolomites* (eds. B. H. Purser, M. E. Tucker and D. H. Zenger). John Wiley & Sons, New York, pp. 133–153.
- Vasconcelos C. and McKenzie J. A. J. (1997) Microbial mediation of modern dolomite precipitation and diagenesis under anoxic conditions (Lagoa Vermelha, Rio De Janeiro, Brazil). *J. Sediment. Res.* **67**, 378–390.
- Vasconcelos C., McKenzie J. A., Bernasconi S., Grujic D. and Tien A. J. (1995) Microbial mediation as a possible mechanism for natural dolomite formation at low temperatures. *Nature* **377**, 220–222.
- Vasconcelos C., Warthmann R., McKenzie J. A., Visscher P. T., Bittermann A. G. and van Lith Y. (2006) Lithifying microbial mats in Lagoa Vermelha, Brazil: modern precambrian relics? *Sediment. Geol.* **185**, 175–183.
- Veizer J., Ala D., Azmy K., Bruckschen P., Buhl D., Bruhn F., Carden G. A. F., Diener A., Ebnet S., Godderis Y., Jasper T., Korte C., Pawellek F., Podlaha O. G. and Strauss H. (1999) $^{87}\text{Sr}/^{86}\text{Sr}$, $\delta^{13}\text{C}$ and $\delta^{18}\text{O}$ evolution of Phanerozoic seawater. *Chem. Geol.* **161**, 59–88.
- Vlahović I., Tišljar J., Velić I. and Matićec D. (2005) Evolution of the Adriatic Carbonate Platform: palaeogeography, main events and depositional dynamics. *Palaeogeogr. Palaeoclimatol. Palaeoecol.* **220**, 333–360.
- Walter B. F., Immenhauser A., Geske A. and Markl G. (2015) Exploration of hydrothermal carbonate magnesium isotope signatures as tracers for continental fluid aquifers, Schwarzwald mining district, SW Germany. *Chem. Geol.* **400**, 87–105.
- Warren J. (2000) Dolomite: occurrence, evolution and economically important associations. *Earth-Sci. Rev.* **52**, 1–81.
- Wilkinson B. and Algeo T. (1989) Sedimentary carbonate record of calcium-magnesium cycling. *Am. J. Sci.* **289**, 1158–1194.
- Wright V. P. (1992) A revised classification of limestones. *Sediment. Geol.* **76**, 177–185.
- Zevin L. S. (1979) Methods of mixing in quantitative X-ray phase analysis. *J. Appl. Cryst.* **12**, 582–584.
- Zhang F., Xu H., Konishi H. and Roden E. E. (2010) A relationship between d104 value and composition in the calcite-disordered dolomite solid-solution series. *Am. Mineral.* **95**, 1650–1656.
- Ziegler M. (2001) Late Permian to Holocene paleofacies evolution of the Arabian Plate and its hydrocarbon occurrences. *GeoArabia* **6**, 445–505.

Associate editor: Fang-Zhen Teng